WWU

Fachbereich 10
Mathematik und
Informatik

Masterarbeit

CutFEM forward modeling for geometries with touching surfaces in bioelectromagnetism

Tim-René Erdbrügger

Matr. 407645

Erstgutachter: Prof. Dr. Carsten Wolters
Zweitgutachter: Prof. Dr. Christian Engwer

Fachbereich für Mathematik und Informatik, University of Münster, Germany

02. März 2021

Contents

List of Figures

1. Introduction

Electroencephalography(EEG) and transcranial direct current stimulation (tDCS) are non-invasive tools in bioelectromagnetism that are used for a wide array of medical purposes. EEG is a tool to measure electric signals caused by brain activity through scalp electrodes. TDCS aims at modulating said activity via electric stimuli applied on the scalp. They both pose a mathematical problem, in EEG one has to localize the origin and strength of an active brain region and in tDCS one has to find adequate positions for the stimulation electrodes. An important part in solving these problems is the so called forward problem, determining the effect of a hypothetical source of brain activity on the EEG-measurement or the effect that an electric stimulus applied at a certain position has on the targeted brain region. To solve the forward problem, two requirements have to be met. A solver algorithm able to simulate electric conduction throughout the head and an accurate depiction of said head to ensure that the simulation corresponds to reality. While the latter is usually ensured by taking MRI-pictures, the Finite Element Method(FEM) has become more and more popular as a solver algorithm over recent years. The subject of this thesis lies in comparing two FEM-approaches, one conventional, state of the art approach and a recently developed CutFEM-approach, with regard to their performance in a scenario where the brain, that is usually floating in a liquid, touches the inner surface of the skull. Scenarios like this are common when the patient is lying down and the brain sinks to the bottom of the head.

After the introduction, Chapter two of this thesis gives an overview of the physiological background of EEG and tDCS, leading up to the Maxwell-equations from which a partial differential equation stating the forward problem is derived. Chapter three sets up a a framework in which this equation can be solved numerically via the two FEM-approaches introduced in the fourth part. The fifth chapter then examines the two methods with regard to differences in their theoretical convergence rate. The evaluation of the touching geometry scenario mentioned above is covered in chapter six. A simplified model is introduced where analytical, quasi-exact, solutions to the forward problems exist as benchmarks for the methods. Finally, the last chapter summarizes the results and gives an outlook.

The Appendix contains complementary information regarding details about a faster computation technique for EEG as well as a description of the model that is used to simulate the electric activity in the brain. Furthermore, brief summaries of the analytical solutions that are used for comparison are stated in addition to an overview of the software that was used for numerical implementations.

2. Physiological Background and Mathematical Basics

This chapter gives a short introduction into how neural activity relates to electric activity. Measuring this activity via electrodes placed on the head surface is called Electroencephalography(EEG). As stated in the introduction, reconstructing the origin of a given EEG measurement is a complex mathematical problem, consisting of multiple involved steps. The first of those is the formulation of a partial differential equation that describes the head as a volume conductor. Its derivation from Maxwell's equations will be covered in this chapter.

A related application which aims at modulating neural activity is Transcranial Direct Current Stimulation (tDCS). A current is injected through scalp electrodes, resulting in an increase or an inhibition of excitability of a target area in the brain. As will be seen, it has a mathematical formulation which is quite similar to the EEG.

The advantage of both the EEG and tDCS is that they are noninvasive, safe and rather easy to conduct. Clinical applications can be tested on healthy subjects first, without the threat of causing permanent damage or considerable side-effects.

2.1. Neural activity in the brain

The human brain consists of about 100 billion neurons([HH09]). Each neuron consists of the same basic parts(see Fig.1). Several Dendrites that connect to the cellbody, the Soma, and an Axon. ([KK09]) The Axon can be imagined as a long tube relaying information in the shape of a so called action potential. Near its end it splits into multiple strains connecting to Dendrites of other neurons. These connections are called synapses. Passed information is either inhibitory or excitatory, depending on the Dendrite. Through synapses received information is relayed by the Dendrite to the Soma where it is summed up. Given sufficiently strong positive signals from its Dendrites, a new action potential emerges at the connection point of Soma and Axon and the signal is passed on.

2.1.1. Resting and Action Potential

A neuron in resting state has an electric potential along its membrane. This is due to the presence of different cations in- and alongside the neuron, namely potassium(K^+), sodium(Na^+), and negatively charged anions like chloride(Cl^-). While potassium mainly resides inside the neuron, the others are found in the exterior. The reason for is the selective permeability of the membrane, mostly preventing potassium from leaving the neuron or the

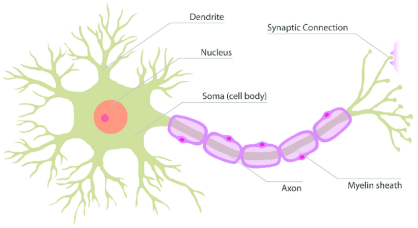

Fig. 2.1.: Structure of a Neuron. Dendrites connect to the Soma and form synapses with other Axons. The Myelin sheath serves to insulate the Axon. ([Fou20])

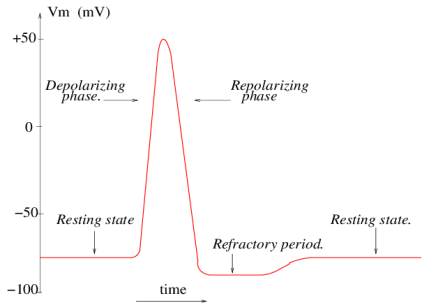

Fig. 2.2.: Illustration of the typical phases of an action potential. ([CS06])

other ions from entering. This concentration disparity is further enhanced by the activity of a potassium-sodium-pump, carrying potassium inside and sodium outside. The resulting resting potential levels off at around -70 mV.

An action potential emerges when the Axon is sufficiently depolarized, an effect that will be explained later on. Within 1 ms this depolarization leads to the opening of channels which allow positively charged sodium to enter the Axon, quickly increasing the membrane potential to around +40 mV and carrying the depolarization further along the Axon. These channels are only open for a short period of time, after which they close on their own. At this point another set of more slowly reacting channels open from the depolarization, allowing potassium to leave the Axon. This leads to a decrease in potential to about -80 to -90 mV at which point all channels are closed again. Now the Axon is filled with large quantities of sodium while potassium is mainly found outside, preventing another depolarization from exciting another action potential. Only after the sodium-potassium-pump has reinstated the resting potential, the Axon is excitable again. This whole process only takes a few milliseconds, the positive spike of the potential only around one millisecond. Unfortunately, this is too short for an EEG to capture. Furthermore, the Axons are usually not lined up nicely leading them to cancel each others signals out, preventing an accurate measurement.([HVG+07])

Thus a different kind of signal has to be investigated. Namely the activity leading up to the action potential, which can be measured nicely.

2.1.2. Postsynaptic Potentials and Pyramidal Cells

An active (presynaptic-)Axon connected via synapse to a (postsynaptic-)Dendrite releases neurotransmitters into the cleft between the two. The transmitters lead to an opening of ion channels in the postsynaptic membrane, thus either depolarizing or hyperpolarizing the Dendrite, depending on the ion charge. This postsynaptic change in electric potential leads to a movement of charged particles towards the Soma, where a sufficiently strong depolarization results in an action potential as mentioned in the previous section. This primary current from synapse to Soma inside the Neuron is set off by an extracellular current in the opposite direction. As the postsynaptic potential has a duration of 10-20 ms, it is long enough for an EEG to measure these current flows. Being actual currents, they give rise to an electric field and a potential that can be measured via electrodes at the

scalp.

However, the problem of orientation remains. A large number of identically oriented neurons would be needed to create a sufficiently strong signal that penetrates the weakly conducting skull. Fortunately, in most parts of the brain a certain group of neurons called Pyramidal Cells can be found. These contain two kinds of Dendrites, basal and apical. While the basal Dendrites emerge radially around the Soma, the apical Dendrite, bascially just a large Dendrite, is oriented normally to the cortical surface. This consistent orientation combined with the longer duration of postsynaptic potentials allows for the activity of sufficiently large clusters of Pyramidal Cells to be measured by an EEG.

The electric potential that can be measured at the scalp is largely influenced by the conductivity of the different head compartments, especially the insulating skull. Furthermore the orientation of the measured neurons is normal to the cortical surface, thus an accurate model of the different compartments is needed in order to achieve accurate results. This is true for the EEG as well as tDCS. ([WAT+06],[WRA+13])

2.2. Foundations of Transcranial Brain Stimulaton

Transcranial electric Stimulation of the brain is an old technique. While in antiquity the electric impulses emitted by torpedo fish held to ones head were used to alleviate headaches([LB86]), more recent methods rely on the injection of electric current through electrodes placed on the scalp. While being noninvasive, without strong averse effects and, when compared to e.g. transcranial Magnetic Stimulation, easy to apply, it has shown to have a measurable effect on neuroplasticity ([FRM+10]), motivating its use in numerous applications from improved learning and memory functions ([GMH+20]) to the treatment of Depression. ([NBFPL09])

At 1-2 mA, the injected currents are not strong enough to cause a sufficient depolarization for the rise of an action potential([BIA+04]). However, they do affect the resting potential of the membrane, increasing or decreasing the necessary depolarization needed for an action potential. It thus modulates the excitability of the targeted cortical region([PBR+98]). Furthermore, the constant electric field has an impact on the ion channels of the neurons, giving rise to a change in the composition of ions present. These changes can remain even after the stimulation ends. TDCS may even have an effect on the interconnectivity of different cortical regions. ([BNB+12])

As tDCS relies on injecting current it gives, similar to the neural activity, rise to an electric eield and potential. Expressing these quantities mathematically requires usage of the Maxwell equations.

2.3. Maxwell equations and the EEG-/tDCS-forward problem

Let E denote the electric field, B the magnetic field, ρ the charge density, J the current density, ϵ_0 and μ_0 the electric permittivity and magnetic permeability. Then the Maxwell equations in differential form in Gaussian Units are

Definition 2.1 (Maxwell Equations)

$$\nabla E = \frac{\rho}{\epsilon_0} \tag{2.1}$$

$$\nabla B = 0 \tag{2.2}$$

$$\nabla \times E = \frac{\partial B}{\partial t} \tag{2.3}$$

$$\nabla \times B = \frac{1}{\mu_0}(J + \epsilon_0 \frac{\partial E}{\partial t}) \tag{2.4}$$

An EEG with 2 electrodes measures the difference in potential energy between two points on the scalp. In Electrostatics, where the time derivatives are zero, this is just the integral of E over an arbitrary path connecting the two. This path-independency allows to define the plectric potential u as a scalar field and the electric field as its derivative.([FW20]) In other words

$$-\nabla u = E. \tag{2.5}$$

In this case, knowing the scalar quantity u translates to complete knowledge of the electric field.

Fortunately, the fields created by the neural activity of the brain or electric stimulation mostly do not exceed 100 Hz ([PH67]). At these lower frequencies, the time derivatives in (2.3) and (2.4) can be neglected. Thus, the electric field is free of rotation and the above mentioned integral path-independent, reducing the problem to finding the scalar potential u.

The next step is to split the current density J into primary J^p and secondary currents J^v, the former originating directly from our electric activity (neurons or stimulation electrodes), the latter being return currents flowing through the head. For these return currents the conductivity of the brain compartments is vital because through Ohm's law for volume conductors they can be described as

$$J^v = \sigma E$$

and thus, using (2.5)

$$J = J^p + J^v = J^p - \sigma \nabla u. \tag{2.6}$$

Here σ is either a constant for isotropic compartments or a positive definite 3×3 tensor for anisotropic areas. Substituting (2.6) into the electrostatic version (2.4) and taking the divergence on both sides yields

$$0 = \nabla(\nabla \times B) = \nabla \epsilon_0 (J^p - \sigma \nabla u),$$

where we used that the divergence of the rotation of a vector field is zero. Transforming the above gives

$$\nabla J^p = \nabla \sigma \nabla u \tag{2.7}$$

over the domain of the head (denoted Ω from now on).

For the EEG, source and sink of the electric current are only separated by the neurons membrane. Also we look at the neuron only from a distance (the scalp), allowing us to approximate the source term J^p by a mathematical point dipole ([HHI+93]). A point dipole can be understood as 2 charges of opposite strength, moved infinitesimaly close together.

Using a Vector M to describe the direction from negative to positive charge and a Dirac-Delta Distribution

$$\delta(x) = \begin{cases} \infty \, , x = 0 \\ 0 \quad , else \end{cases}$$

and

$$\int_{-\infty}^{\infty} \delta(x) dx = 1$$

the source term for a dipolar source at a given point x_0 can be written as

$$J^p(x) = M\delta(x - x_0), \tag{2.8}$$

where M is the dipole moment or "Direction". Now, only the question of boundary conditions has to be answered to fully state the EEG and tDCS forward problems.

Definition 2.2 (EEG forward problem) *For the EEG case we can employ homogenous Neumann boundary conditions, since the head can be considered as an electric insulator and the air is not conductive. Thus the EEG forward problem is stated as*

$$\nabla\sigma\nabla u = \nabla J^p \quad in\, \Omega \tag{2.9}$$

$$\langle \sigma\nabla u, n\rangle = 0 \quad on\, \partial\Omega, \tag{2.10}$$

where n is the outer unit normal.

The final goal of EEG source analysis is to find the set of sources that best matches the signal that is measured via electrodes at the scalp. It is thus necessary to calculate the solution to the forward problem for a large set of sources spread throughout the brain, evaluate their respective potential at the electrode positions and then find a matching source configuration. Solving the last part is called the inverse problem of the EEG. Forward modeling thus aims at providing an accurate Lead-Field, i.e. a matrix $L \in \mathbf{R}^{s\times 3N}$ (s electrodes, N source locations) such that $L_{i,j}$ is the potential value at electrode i caused by a source in $x-, y-$ or z- direction (Superposition states that any source direction can be split into its x, y, z components). L can then be multiplied with a source configuration $x \in \mathbb{R}^{3N}$ to obtain a vector containing the cumulative potential value for each electrode.

Definition 2.3 (tDCS forward problem) *In tDCS, we can skip the source term J^p and model the injection of current as two delta distributions, one of them with negative sign for the sink electrode, acting on the boundary. Aside from these, the same homogeneous Neumann boundary conditions as for the EEG can be applied. Thus, the TDCS-forward problem is stated as*

$$\nabla\sigma\nabla u = 0 \quad in\, \Omega \tag{2.11}$$

$$\langle \sigma \nabla u, n \rangle = I \quad \text{on } \partial\Omega, \tag{2.12}$$

where $I = \delta(x - x_0) - \delta(x - x_1)$ *is the current pattern injected at position* x_0 *and* x_1.

Similar to the EEG case, solving the tDCS forward problem is only the precursor to the inverse problem of finding the electrode configuration that maximizes the electric current in the brain are one wants to target. One is thus also interested in computing a matrix $T \in \mathbb{R}^{s \times 3N}$, this time containing the current flow at specific locations in $x-, y-$ and $z-$direction. In this thesis the focus lies exclusively on accurate forward modeling.

This concludes the chapter. The following ones will focus on deriving a scheme to solve these differential equations.

3. Weak formulation, Existence and Uniqueness

While the aforementioned forward problems can be solved in the classical sense they were stated in before, the requirements for the existence of such a solution are rather high. Especially a continuous conductivity tensor σ is required. Unreasonable, as σ varies strongly across the different compartments of the head ([VCR+14]) and there are no large transition areas. Thus, the conductivity jumps.

In order to deal with these jumps, the forward problems are transformed to a weak formulation. From this state it is possible to derive statements about the existence of unique solutions of the equations.

3.1. Weak Formulation

The idea is to multiply each side of the equation with some kind of later defined testfunction v, followed by an integration over Ω. From here one can employ partial integration to shift the differential operators over from our solution u to the testfunction. Solving the resulting integral equation has the advantage that no requirements regarding the differentiability of u are made, allowing for solutions that are not differentiable in the classical sense. As the name of the formulation suggests, these are called weak solutions.

In the following, a derivation of the weak formulation of the tDCS forward problem and the existence of a unique solution will be stated. The EEG case is identical in most and similar in the other steps and will therefore only be stated at the end. The procedure roughly follows ([WKM+07]) and ([WBW15]). Starting at equation (2.11) of the tDCS forward problem, multiplication with a function $v \in V$ and integrating over Ω yields

$$\int_\Omega (\nabla\sigma\nabla u)v dx = 0.$$

Partial integration then results in

$$-\int_\Omega \sigma\nabla u\nabla v dx + \int_{\partial\Omega} \langle\sigma\nabla u, n\rangle v dS = 0.$$

And finally, using the boundary condition from (2.12) we obtain

$$\int_\Omega \sigma\nabla u\nabla v dx = \int_{\partial\Omega} I v dS. \tag{3.1}$$

As the solution should not depend on which testfunction is used, (3.1) should be true for as general a v as possible. Thus, a prudent definition of the vector space V is needed. It is

also necessary to specify to which class of functions u is supposed to belong. This is needed to make statements regarding the existence of a solution and for formulating the numerical approximation that is computed later on.

The usual approach is to define V to be a Sobolev Space, in this case a subspace of $H^1(\Omega)$. For a short overview and motivation, see Appendix B, for a more detailed description, see ([Eva14]).

As equation (3.1) is only unique up to a constant, we also require that the Potential has zero mean over the entire head or in other words

$$\int_\Omega u dx = 0.$$

Thus we choose

$$V = H^1_*(\Omega) := \{v \in H^1(\Omega) : \int_\Omega v dx = 0\}.$$

As closed linear subspace of a Hilbert Space this is also a Hilbert Space. When treating the equation numerically one usually fixes one value on the boundary and subtracts the mean potential afterwards. Now it is possible to fully state the tDCS and EEG forward problem:

Definition 3.1 (weak tDCS forward problem) *find $u \in H^1_*(\Omega)$ such that*

$$\int_\Omega \sigma \nabla u \nabla v dx = \int_{\partial\Omega} I v dS \ \ \forall v \in H^1_*(\Omega). \tag{3.2}$$

Definition 3.2 (weak EEG forward problem) *find $u \in H^1_*(\Omega)$ such that*

$$\int_\Omega \sigma \nabla u \nabla v dx = -\int_\Omega \nabla J^p v dS \ \ \forall v \in H^1_*(\Omega). \tag{3.3}$$

3.1.1. Existence and Uniqueness of a solution

We proceed with the tDCS case and define

$$a : V \times V \to \mathbb{R}, \ (u, v) \mapsto \int_\Omega \sigma \nabla u \nabla v dx \tag{3.4}$$

$$l : V \to \mathbb{R}, \ v \mapsto \int_{\partial\Omega} I v dS. \tag{3.5}$$

In order to apply Lax-Milgram (see Theorem $B.1.$), we need a to be continuous and coercive and l to be part of $H^1_*(\Omega)'$.

Lemma 3.1 *a is continuous and coercive.*

Proof: As a is bilinear, it suffices to show boundedness in V. Let σ_{max} be the largest eigenvalue of σ. Then

$$|a(u, v)| = |\int_\Omega \sigma \nabla u \nabla v dx| \leq \sigma_{max} \int_\Omega ||\nabla u||_2 ||\nabla v||_2$$

$$\leq \sigma_{max}||u||_{L^2}||\nabla v||_{L^2} \leq \sigma_{max}||u||_{H^1}||v||_{H^1},$$

where Hölder's inequality was used. Therefore a is bounded and continuous if σ's largest eigenvalue is finite.

For coerciveness we first need a variant of Friedrich's inequality([Bra07]): Let $\Omega \subseteq \mathbb{R}^n$ be contained in a cube with edge length s. Then for each u in $H^1(\Omega)$

$$||u||_0 \leq |\bar{u}|\sqrt{\mu(\Omega)} + 2s|u|_1,$$

where $\bar{u} = \int_\Omega u dx/\mu(\Omega)$. With σ_{min} being the smallest eigenvalue of σ one obtains for any $u \in H^1_*$

$$a(u,u) \geq \sigma_{min}\int_\Omega ||\nabla u||_2^2 = \frac{\sigma_{min}}{1+4s^2}(|u|_1^2 + 4s^2|u|_1^2)$$

$$\overset{\bar{u}=0}{=} \frac{\sigma_{min}}{1+4s^2}(|u|_1^2 + (\bar{u}\sqrt{\mu(\Omega)} + |u|_1)^2)$$

$$\geq \frac{\sigma_{min}}{1+4s^2}(|u|_1^2 + ||u||_0^2) = \frac{\sigma_{min}}{1+4s^2}||u||_1^2.$$

Thus a is coercive.

□

In order for l to be part of $H^1(\Omega)'$ the trace theorem $(B.2)$ is employed.

Lemma 3.2 *If $I \in H^{-\frac{1}{2}}(\partial\Omega)$ in the sense that $I(v) = \int_{\partial\Omega} IvdS$, then l is well defined and bounded in $H^1(\Omega)$.*

Proof: $I \in H^{-\frac{1}{2}}(\partial\Omega)$ implies that

$$l(v) = I(T(\bar{v})), \text{ for some } \bar{v} \in H^{\frac{1}{2}}(\partial\Omega).$$

Then by the trace theorem we have

$$|l(v)| \leq \int_{\partial\Omega} |IT(v)|dS = \int_{\partial\Omega} I\bar{v}dS$$

$$\leq ||I||_{H^{-\frac{1}{2}}(\partial\Omega)}||v||_{H^{\frac{1}{2}}(\partial\Omega)} \leq C||I||_{H^{-\frac{1}{2}}(\partial\Omega)}||v||_{H^1(\Omega)}.$$

□

As the dirac delta functions used to describe I are part of H^{-s} for any s larger than $n/2$, they are also part of $H^{-\frac{1}{2}}(\partial\Omega)$.

Therefore, we can apply Lax-Milgram to justify the existence of a unique solution to the weak tDCS-forward problem.

The bilinearform a is identical for EEG and tDCS, thus the proof mostly extends to the EEG-case. However, proving that l fullfills the necessary requirements is a little more troublesome. This is due to the singularity in the primary current J^p. In ([WKM$^+$07]) a subtraction approach is presented, splitting the conductivity into a sum of two independent ones. One anisotropic part that is zero at the location of the dipole and another one that is constant over the entire domain to correct for the zero conductivity of the first.

For the remainder of this thesis modeling the sources will follow the principle of St. Venant (see A.2.). It has the advantage of being very accurate and already available for both FEM-approaches that will be investigated in this thesis.

The weak formulation is the starting point for numerically solving the EEG and tDCS forward problem. The FEM approaches used for this will be described in the following chapter.

4. The Finite Element Method

The finite element method (FEM) is a numerical procedure to treat partial differential equations. Its use is widely spread throughout the natural sciences with numerous applications in fields like electromagnetism, heat transfer, fluid flow, etc..

While different variants of the method exists, the principles are mostly identical. The goal is to solve a weakly formulated PDE on a given geometry by approximating the solution in a finite-dimensional vector space. The first step is to simplify the geometry by replacing it with a mesh, i.e. many disjunct elements of a simple structure, for example tetrahedrons or hexahedrons in 3D. On each of these, a number of functions is defined. These are the finite elements from which the method derives its name. Their linear combinations form a finite dimensional vector space in which the solution to the PDE can be approximated. To do this, both solution and testfunctions are projected into the vector space, i.e. they are replaced by a linear combination of the finite elements (one can have different spaces for solution and testfunctions, the functions approximating the solution are called Ansatzfunctions). The PDE then reduces to finding the coefficients of said combination, meaning one has to solve a linear equation system. The described process is generally called Galerkin-Method.

The remainder of this chapter is split into two parts, the first explaining a standard tetrahedral Continuous-Galerkin (CG-)FEM approach, the second being a Cut FEM, whose performance when compared to the first is subject of this thesis. A short numerical analysis of both versions will follow in the next chapter.

4.1. Conforming Tetrahedral Continuous Galerkin

For the purposes of EEG and tDCS one mostly uses either a realistic head model, segmented from Magnetic Resonance Imaging, or a sphere model (see Figure 4.1.). The advantage of the latter is the existence of analytical solutions([DM88], [FET00]). Thus, they are well suited to test the accuracy of numerical algorithms before proceeding with the actual realistic head. Using tetrahedrons as the basic element to form the mesh has the advantage that curvatures can be more accurately modelled. A hexahedral mesh follows curves in a staircase pattern, which is problematic when modelling the thinner parts of the skull (see Fig 4.2.). There are ways to deal with this, for example adaptive meshing or the discontinuous Galerkin method. However, these methods are mostly not better than simply using a tetrahedral mesh([EVLW17]) and will thus not be considered here. The head can be split into several non-overlapping compartments or domains, e.g. the scalp, skull, cerebrospinal fluid (CSF), white and grey matter. In other words

$$\Omega = \bigcup_i \Omega_i$$

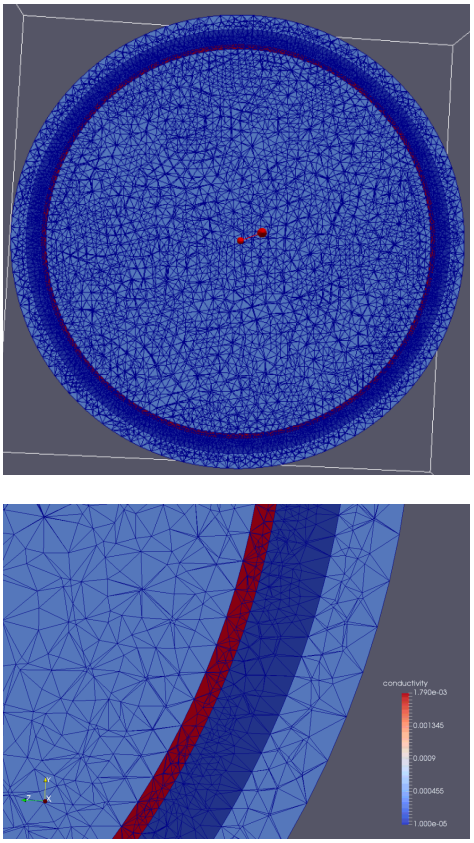

Fig. 4.1.: Example of a 4-layer sphere model using a tetrahedral mesh. Different mesh resolutions for the compartments yield an exact representation of the sphere while saving on computation time.

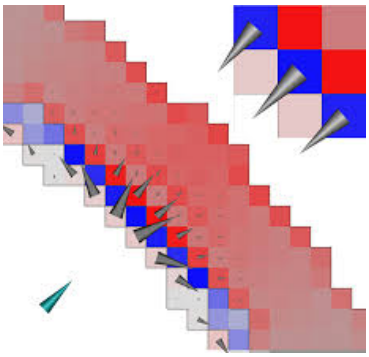

Fig. 4.2.: Visualization of possible Skull leakage effect in a hexahedral mesh. The thin skull compartment(blue) allows current (cones) to leak through the gaps of the staircase, diminishing the insulating effect of the skull.([EVLW17])

with Ω being the entire head and Ω_i the different domains. Then by $\mathcal{T} = \{E_k\}_{k \in K}$ one can denote a mesh consisting of a finite set of tetrahedrons such that

$$\Omega \subset \bigcap_{k \in K} E_k \text{ and } \mu(E_k \cap E_j) = 0 \text{ for } k \neq j.$$

Here μ is used as the 3D-Lebesgue measure.

Normally, one uses a tool like gmsh([GR09]) to create the mesh. It first meshes the surfaces and from there the complete volume for every compartment. Thus, each compartment is represented without overlap by the tetrahedrons belonging to it.

As functions to approximate the solution the Lagrange-Interpolation is used: For this purpose let

$$V_h = \{v \in H_0^1(\Omega) : v|_{E_k} \text{ is polynomial of degree 1 for all } k \in K\}.$$

This is the vector space from which both solution and testfunctions will be derived. For proper usage of V_h a basis is needed:

Let N denote the number of nodes or vertices of the mesh. Then for each node x_i a linear Ansatzfunction ϕ_i is defined such that

$$\phi_i(x_j) = \delta_{ij}. \tag{4.1}$$

Given the above property, any function u can be interpolated using its value at the N positions $(x_i)_i$. As a linear approximation of u one can simply write

$$u_{approx}(x) = \sum_{i=1}^{N} u(x_i)\phi(x).$$

From (4.1) one obtains

$$u(x_i) = u_{approx}(x_i) \; \forall \; i = 1, ..., N$$

and thus an approximation that is exact on the nodes.

Giving an exact formula for each Ansatzfunction would be a bit technical. Instead it has proven practical not to define each ϕ_i explicitly but rather by associating them with the tetrahedrons whose edges they represent. Each tetrahedron is then just a distorted version of some basic, evenly shaped reference tetrahedron onto which the original one can be mapped. More precisely:

Given a tetrahedron E_k, an invertible linear mapping

$$M_k : E \mapsto \hat{R}$$

to the reference element $\hat{R}$ can be defined. On this $\hat{R}$, that has the vertices

$$\begin{bmatrix}0\\0\\0\end{bmatrix}, \begin{bmatrix}1\\0\\0\end{bmatrix}, \begin{bmatrix}0\\1\\0\end{bmatrix}, \begin{bmatrix}0\\0\\1\end{bmatrix}, \tag{4.2}$$

functions can be defined according to

- $\psi_1(x, y, z) = 1 - x - y - z$

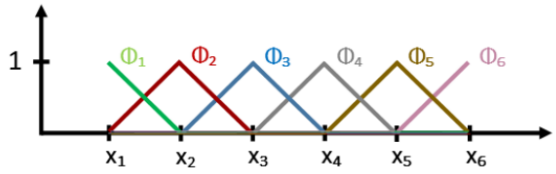

Fig. 4.3.: Schematic portrayal of Ansatzfunctions ([Kra19])

- $\psi_2(x, y, z) = x$
- $\psi_3(x, y, z) = y$
- $\psi_4(x, y, z) = z$.

These functions fulfill (4.1) and can therefore each be assigned to one vertex of $\hat{R}$. The value of an Ansatzfunction ϕ_i at a position inside the tetrahedron can then be computed as

$$\phi_i(x) = M^{-1}(\psi_j(M_k(x))).$$

The resulting ϕ_i's then look like hat functions, a 1D-representation can be seen in (see Fig. 4.3.). Any piecewise polynomial function $v \in V_h$ can now be seen as a linear combination of the ϕ_i and thus

$$V_h = span(\{\phi_i : i = 1, ..., N\}).$$

Having defined the Ansatzfunctions, one can proceed solving the differential equation. Substituting an approximation

$$u_h(x) = \sum_{i=1}^{N} c_i\phi_i(x), \quad c_i \in \mathbb{R}$$

from (4.1) (the h represents how fine the mesh is, e.g. the diameter of the tetrahedrons) into the bilinear form a from (3.4), one obtains

$$a(u_h, v) = \int_\Omega \sigma\nabla(\sum_{i=1}^{N} c_i\phi_i(x))\nabla v dx = \sum_{i=1}^{N} c_i \int_\Omega \sigma\nabla\phi_i\nabla v dx.$$

Instead of solving the weak forward problem

$$a(u_h, v) = l(v) \tag{4.3}$$

for each $v \in H_0^1(\Omega)$, the equation is narrowed down to the piecewise polynomials defined earlier, i.e. to each $v \in V_h$. l can be either from the tDCS or EEG version.

As each v is now a linear combination of the basis functions ϕ_i it suffices to show that (4.3) holds for these basis functions. Thus, N equations

$$a(u_h, \phi_j) = l(\phi_j) \tag{4.4}$$

for $j = 1, ..., N$ are obtained.

These equations can be written neatly using a stiffness matrix and 2 vectors:

Let $K \in \mathbb{R}^{N\times N}$ have the indices

$$k_{ij} = \int_\Omega \sigma \nabla \phi_i \nabla \phi_j dx$$

and $u, b \in \mathbf{R}^N$ be defined by

$$u_i = c_i,\ i = 1, ..., N$$
$$b_i = \int_{\partial\Omega} I\phi_i dS,\ i = 1, ..., N.$$

Then solving (4.4) is equivalent to solving the linear equation system

$$Ku = b. \tag{4.5}$$

Note that the integral terms in the entries of(4.5) can easily be computed as each Ansatzfunction is non-zero only for the few elements bordering its node.

4.2. A Cut Finite Element Method

Standard fitted FEM approaches like the one previously presented create a mesh that is specifically tailored to the geometry. In unfitted approaches like CutFEM one uses a fundamental mesh that is independent of the geometry. This mesh is then cut by level-set functions that characterize the surfaces of each compartment to be modeled. This cut runs not along the boundaries of each mesh element but right through them. Thus some elements are cut into multiple snippets or cut-cells with a geometry different from the original element.

This new cut mesh can be divided into one submesh for every compartment and finite element functions can be defined in a manner identical to the CG-FEM on each of them. To ensure that these independent Ansatzfunctions yield a solution that does not contain jumps one has to sort of glue them together. This is achieved by adding penalty terms for jumps to the bilinearform into which the Ansatzfunctions are substituted.

4.2.1. Fundamental mesh and Level-Set Function

Similar to before, the head domain Ω consists of a set of disjunct subdomains Ω_i. Next, a larger domain $\hat{\Omega}$ containing Ω can be defined. For the sake of simplicity we choose $\hat{\Omega}$ to be a cube. On this larger domain the fundamental mesh is defined. As it is not required to accurately represent the head geometry, one can pick a simple shape that is uniform over all elements, in this case hexahedrons.

Thus let $\mathcal{T}(\hat{\Omega}) = \{E_k\}_{k\in K}$ be a set of non-overlapping, uniform hexahedrons such that

$$\bigcup_{k\in K} E_k = \hat{\Omega}.$$

To characterize the different domains, continuous level set functions $\Phi_i : \hat{\Omega} \mapsto \mathbb{R}$ can be defined such that

$$\Phi_i(x) \begin{cases} < 0, \text{ if } x \in \Omega_i \\ = 0, \text{ if } x \in \partial\Omega_i \\ > 0, \text{ else.} \end{cases}$$

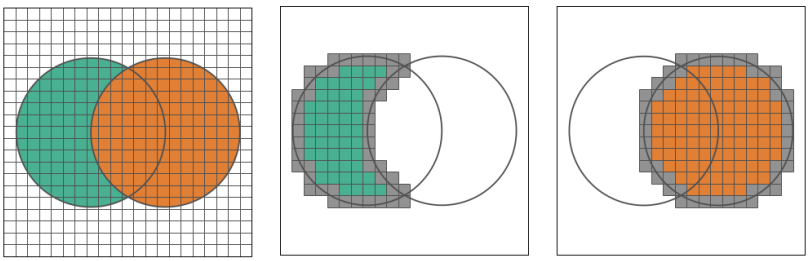

Fig. 4.4.: Left: two given domains and a fundamental background mesh. Middle, right: The respective submeshes for domain 1 and 2. Grey elements indicate an overlap into the other domain/the outside. ([Nüß18])

For each domain, the level-set $\{x \in \hat{\Omega} : \Phi_i(x) = 0\}$ can now be laid over the fundamental mesh. A submesh $\mathcal{T}^i$ containing all elements that are either completely inside Ω_i or cut by the level set is then defined.

$$\mathcal{T}^i = \{E_k \in \mathcal{T} : E_k \cap \Omega_i \neq \emptyset\}$$

Note that these meshes overlap (see Fig. 4.4.). This makes defining Ansatzfunctions easier than having to do so on the possibly misshapen snippets. While those functions are defined over the area of a different domain, they will simply be ignored there.

As mentioned in the introduction, each submesh is then equipped with a corresponding finite element space V_h^i. The procedure for this is identical to the one presented in section 4.1, the only difference being the usage of hexahedrons rather than tetrahedrons. This leads to different, but still linear Ansatzfunctions. For information about hexahedral Ansatzfunctions, see ([Bra07]).

Given the FEM-spaces V_h^i one can define

$$V_h = \prod_i V_h^i$$

as overarching FEM-space used for approximating the solution. We then slightly modify the EEG and tDCS forward problems to account for this different vector space.

For any $v_h \in V_h$ let v_h^i denote the restriction of v_h to Ω_i. (3.4.) was obtained by partial integration in (3.1). As Ω is split into multiple domains, each having functions defined on them, that same partial integration now yields additional terms on the interior boundaries or skeleton, defined discretely as

$$\Gamma = \{E \cap (\Omega_i \cap \Omega_j) : E \in \mathcal{T}(\hat{\Omega}),\ i \neq j,\ \mu_2(E \cap (\Omega_i \cap \Omega_j)) > 0\} \tag{4.6}$$

with μ_2 being the two-dimensional Lebesgue-measure.

4.2.2. Nitsche coupling

At this point the restrictions are uncoupled, meaning that there could be discontinuities or jumps over the skeleton. The weak coupling used here is motivated by the Nitsche Method([Nit71]). In its implementation it is analogue to the way Ansatzfunctions are glued

together in the Discontinuous Galerkin Method ([ABCM02]), by penalizing jump terms in the weak formulation of the PDE.

First, we need a suitable jump function that is defined over the skeleton Γ.

Definition 4.1 (Jump function) *Given two disjunct open sets $E, F \subseteq \Omega$, $\bar{E} \cap \bar{F} \neq \emptyset$, a vector-valued function v or a scalar function u, the jump on the interface between E and F is defined as*

$$[\![v]\!] := \langle v|_E, n_E\rangle + \langle v|_F, n_F\rangle \tag{4.7}$$

$$[\![u]\!] := u|_E n_E + u|_F n_F. \tag{4.8}$$

Using this, we can account for possible jumps by extending the tDCS forward problem from (2.11.-12.).

Definition 4.2 (CutFEM tDCS forward problem) *Let Ω be split into m disjunct areas Ω_i. Then the strong forward problem can be stated as*

$$\nabla\sigma\nabla u = 0, \quad in \ \bigcup_i \Omega_i \tag{4.9}$$

$$\langle\sigma\nabla u, n\rangle = I, \quad on \ \partial\Omega \tag{4.10}$$

$$[\![u]\!] = 0, \quad on \ \Gamma \tag{4.11}$$

$$[\![\sigma\nabla u]\!] = 0, \quad on \ \Gamma \tag{4.12}$$

The third term ensures that the electric potential is continuous over internal boundaries (a requirement from electrostatics ([Fli05])) and the last enforces local conservation of charge, i.e. charge that leaves one domain over a boundary actually ends up in the adjacent domain.

Note that the CutFEM changes to the EEG problem are identical.

A similar procedure as in section 2 is used to attain a weak formulation. Multiplying with a testfunction v_h (split into restrictions), integrating over the subdomains and applying partial integration yields

$$\begin{aligned}\int_\Omega \nabla\sigma\nabla u_h v_h dx &= \sum_i \Big(\int_{\Omega_i} \sigma\nabla u_h^i \nabla v_h^i dx - \int_\Gamma \langle\sigma\nabla u_h^i, n\rangle v_h^i dS\Big) - \int_{\partial\Omega} I v_h dS \\ &= \sum_i \Big(\int_{\Omega_i} \sigma\nabla u_h^i \nabla v_h^i dx\Big) - \int_\Gamma [\![\sigma\nabla u_h v_h]\!] dS - \int_{\partial\Omega} I v_h dS. \end{aligned} \tag{4.13}$$

The last step adds up the two integral terms that exist for each interior boundary, one per adjacent domain.

To enforce the first jump condition, a helper function is introduced:

Definition 4.3 (weighted and skew-weighted average) *Given 2 disjunct open sets $E, F \subseteq \Omega$, $\bar{E} \cap \bar{F} \neq \emptyset$, a scalar or vector-valued function u, the weighted average on the interface between E and F is defined as*

$$\{u\} = \omega_E u|_E + \omega_F u|_F \tag{4.14}$$

with

$$\omega_E = \frac{\delta_E}{\delta_E + \delta_F}$$
$$\delta_E = n_E^t \sigma_E n_E.$$

Here, n_E, n_F are the respective outer unit normals, σ_E the positive definite, symmetric conductivity tensor on E.

ω_F and δ_F are defined analogously and the skew weighted average is defined as

$$\{u\}^* = \omega_F u|_E + \omega_E u|_F. \tag{4.15}$$

Using this weighted average, the jump in (4.13) can be simplified using to the following lemma.

Lemma 4.1 *The jump $[\![.]\!]$ of the product of two functions u and v over an interface can be split according to*

$$[\![uv]\!] = [\![u]\!]\{v\}^* + \{u\}[\![v]\!]. \tag{4.16}$$

Proof: [[Nüß18]] Note that $\omega_E + \omega_F = 1$ and $n_E + n_F = 0$. Then simply reordering terms yields

$$\begin{aligned}
[\![u]\!]\{v\}^* + \{u\}[\![v]\!] &= (u|_E n_E + u|_F n_F)(\omega_F v_E + \omega_E v_F) + (\omega_E u_E + \omega_F u_F)(v|_E n_E + v|_F n_F) \\
&= u|_E n_E(\omega_F v|_E + v|_E \omega_E) + u|_F n_F(\omega_E v|_F + v|_F \omega_F) \\
&\quad + u|_E \omega_E v|_F(n_E + n_F) + u|_F \omega_F v|_E(n_F + n_E) \\
&= u|_E n_E v|_E + u|_F n_F v|_F = [\![uv]\!]
\end{aligned}$$

□

Thus, the integral over the skeleton in (4.13) can be rewritten as

$$\int_\Gamma [\![\sigma \nabla u_h v_h]\!] dS = \int_\Gamma [\![\sigma \nabla u_h]\!]\{v_h\}^* + \{\sigma \nabla u_h\}[\![v_h]\!] dS = \int_\Gamma \{\sigma \nabla u_h\}[\![v_h]\!] dS,$$

where the third line of the CutFEM forward problem was used.

Adding or subtracting a symmetry term

$$\Theta \int_\Gamma \{\sigma \nabla v_h\}[\![u_h]\!],\ \Theta \in \{-1, 1\}$$

is done to ensure the (non-)symmetry of the final bilinearform. The two versions differ in their respective approximation properties and the coercivity of the final bilinearform as will be discussed later.

To stabilize the method and to enforce that the potential is jump-free, a penalty term P_γ is added.

$$P_\gamma(u, v) = \gamma \nu_k \int_\Gamma \frac{\hat{\sigma}}{\hat{h}} [\![u_h]\!][\![v_h]\!] dS \tag{4.17}$$

- $\nu_k = k(k+d-1)$ depends on the degree k of the polynomials used and the dimension d of Ω.
- $\hat{\sigma} = \frac{2\delta_E\delta_F}{\delta_E+\delta_F}$ weighs the jump term with the conductivity difference ($\delta_{E,F}$ are defined as in Definition 4.3).
- $\hat{h} = \frac{\min(\mu(E),\mu(F)}{\mu_2(\bar{E}\cap\bar{F})}$ weighs each term with the ratio of the smaller volume of the involved elements E, F and the area of their interface.
- γ is a penalty constant and can be freely chosen but has to be of a certain size least the whole method would not be stable.

The choice and motivation for these parameters are discussed in ([DPE12], [GHH07]).

In total, the Nitsche coupling terms with Symmetric Weighted Interior Penalty Galerkin (SWIPG) are stated as

$$a_s^N(u_h, v_h) := -\int_\Gamma \{\sigma\nabla u_h\}[\![v_h]\!] - \int_\Gamma \{\sigma\nabla v_h\}[\![u_h]\!]dS + \gamma\nu_k \int_\Gamma \frac{\hat{\sigma}}{\hat{h}}[\![u_h]\!][\![v_h]\!]dS, \tag{4.18}$$

or in the Non-Symmetric (NWIPG) case as

$$a_n^N(u_h, v_h) := -\int_\Gamma \{\sigma\nabla u_h\}[\![v_h]\!] + \int_\Gamma \{\sigma\nabla v_h\}[\![u_h]\!]dS + \gamma\nu_k \int_\Gamma \frac{\hat{\sigma}}{\hat{h}}[\![u_h]\!][\![v_h]\!]dS, \tag{4.19}$$

the two only differing in one sign.

From (4.13), the bilinearform a is taken as

$$a(u_h, v_h) = \sum_i \int_{\Omega_i} \sigma\nabla u_h^i \nabla v_h^i dx \tag{4.20}$$

while the right-hand-side term l remains identical to (3.5).

Considering only the restrictions of u_h, v_h to the respective domains resolves the submesh overlap. Now however, depending on the way the level sets cut the fundamental mesh, there might be sliver- or point-like cut-cells. Defining Ansatzfunctions that act only on these tiny, misshapen cells can result in a deterioration of the conditioning and stability of the method([Bur10]).

Alleviating this problem can be done by coupling the gradient of functions inside cut-cells with the gradients of neighboring functions. In other words, the behavior on the inner, uncut cells of the domain is extended to the cut-cells by penalizing the jump of the gradient on the interfaces between cut-cells and inner cells.

The interfaces of all cut-cell with their neighboring cells is given by

$$\hat{\Gamma} = \{\bar{E}_i \cap \bar{E}_j : E_i, E_j \in \mathcal{T}(\hat{\Omega}),\ i \neq j,\ \mu_2(\bar{E}_i \cap \bar{E}_j) > 0,\ E_i \text{ and/or } E_j \text{ is cut by a level set}\}. \tag{4.21}$$

Then the Ghost-penalty term can be stated as

$$a^G(u_h, v_h) = \gamma_G \int_{\hat{\Gamma}} \hat{h}[\![\sigma\nabla u_h]\!][\![\nabla v_h]\!]dS. \tag{4.22}$$

$\hat{h}$ is the same as in (4.17) and γ_G can again be chosen relatively freely. As the penalty is supposed to primarily act on small cut-cells, γ_G is usually much smaller than the penalty

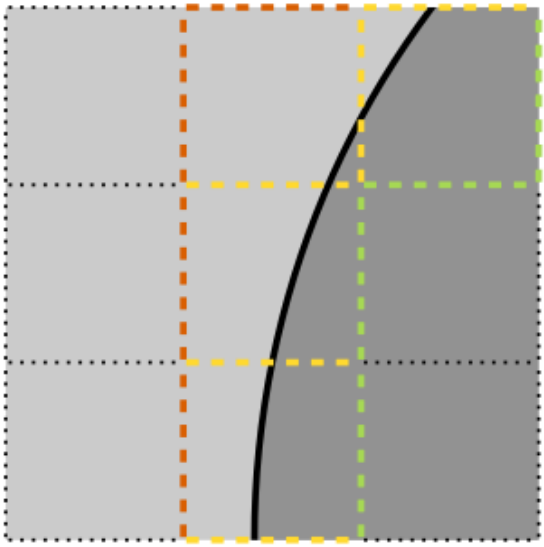

Fig. 4.5.: Overview of the applied penalties. On the level-set (black line), the regular Nitsche-penalty term is used. The dashed colored lines indicate Ghost-penalties. Red for the left domain, green for the right and yellow for penalty terms that affect both domains. ([Nüß18])

parameter γ from the Nitsche-penalty. Fig. 4.5. gives an overview of the different penalties applied.

In total, the above considerations lead to the following definition.

Definition 4.4 (weak tDCS-/EEG CutFEM formulation) *Find $u_h \in V_h$ such that*

$$a(u_h, v_h) + a^N_{n/s}(u_h, v_h) + a^G(u_h, v_h) = l(v_h) \; \forall v_h \in V_h \tag{4.23}$$

with

- $l(v_h) = \int_{\partial\Omega} I v_h dS$ *for tDCS and*
- $l(v_h) = -\sum_i \int_{\Omega_i} \nabla J^p v_h^i dx$ *for EEG.*

This equation leads to a linear equation system similar to (4.5).

One practical issue remains before proceeding to the numerical analysis of the method. Computing the terms in (4.23) requires evaluating integrals over the boundary Γ and the cut-cells. As the level-Set has no restrictions regarding its geometry, those might be of arbitrary shape and thus their computation is not as straightforward as if they where e.g. tetrahedrons.

4.2.3. Cut-cell Integration

As a means for computation, a topology preserving marching cubes (TPMC) algorithm([EN17]) is employed. The idea is to find a set of polygons to replace the cut-cell. The result is a linearized cut-cell that both accurately represents the original one and allows for easy integration via quadrature points. The algorithm basically consists of two approximations, it will be briefly sketched for one domain.

A domain Ω, contained in a larger auxiliary domain $\hat{\Omega}$, is characterized by a level-set function Φ as stated in the beginning of the section. First, the auxiliary domain is tesselated by

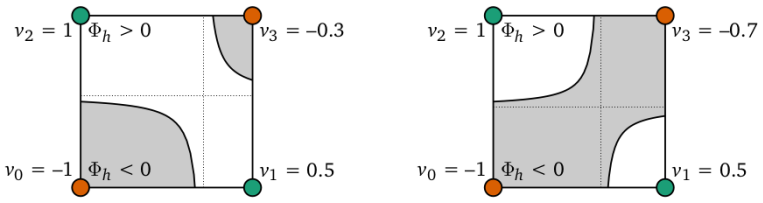

Fig. 4.6.: Ambiguous sign-based key. Both pictures have the same edge values, resulting in the same key. The tube connecting v_0 and v_3 on the right is ignored. Thus further distinctions have to be made ([Nüß18]).

a hexahedral mesh. In the following we always consider one hexahedron at a time. The level-set function is replaced by a multilinear version Φ_h. Multilinear in the sense that the restriction to the cube is supposed to be multilinear. This restriction is uniquely defined by its values on the vertices. It will thus only be used implicitly.

The next step is finding a set of polygons to approximate the area inscribed by Φ_h. These replacements are not computed individually for each cut-cell, instead the best fitting template is chosen from a lookup table. To select that template, first a key is computed that is based on the sign of ϕ_h on the vertices. As there are 8 vertices, there are 2^8, so 256 possible combinations, each represented by one key. Some of those combinations are just rotations or axial mirroring of other combinations and can thus be considered as the same.

However, while some of the keys can result from one kind of level set topology only, others are not unique as can be seen in Fig. 4.6. To preserve the topology of the original level-set, one has to account for possible tubes running through the hexahedron. The existence of such a tube can be determined using the vertex values. For more information regarding the exclusion of this case, see [EN17] and [Tch96].

Having accounted for these ambiguities in topology, one has a template set of polygons E_i^j to replace the original cube E_i. An example of this can be seen in Fig. 4.7.. In summary, the process of integrating over a domain Ω, characterized by a level-set function Φ looks like this:

$$\int_\Omega f dx = \int_{\hat{\Omega}\cap\{\Phi<0\}} f dx = \sum_i \int_{E_i\cap\{\Phi<0\}} f dx$$
$$\approx \sum_i \int_{E_i\cap\{\Phi_h^i<0\}} f dx \approx \sum_i \sum_j \int_{E_i^j} f dx.$$

First, Ω is embedded in the auxiliary domain $\hat{\Omega}$, then the integral is written as a sum of integrals over the cubic mesh of $\hat{\Omega}$. On each cube a multilinear level-set approximation Φ_h^i is defined and finally those integrals are approximated by integrals over the replacement polygons E_i^j. The result can be refined by reapplying the algorithm to the new subtesselation, yielding an a more precise approximation of the domain. Note that this refinement does not affect the number of Ansatzfunctions, which only depends on the fundamental mesh.

A mesh cut by multiple level-set functions can be treated iteratively, each iteration applying the TPMC-Algorithm to the subtesselation created by the previous one.

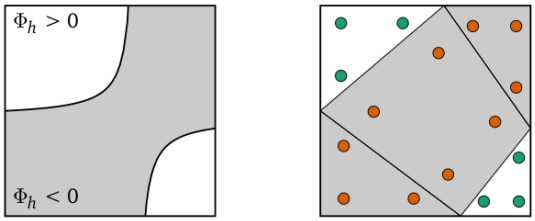

a) Reconstruction of one cut element([Nüß18])

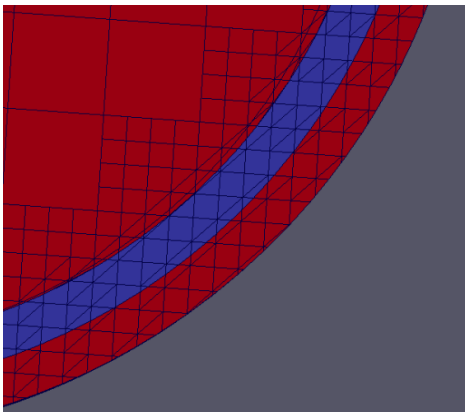

b) Reconstruction of a multilayer sphere model.

Fig. 4.7.: a) Reconstruction of a single square cut by a level-set. The grey area indicates the inside of the domain, reconstructed into 5 cut-cells, 3 of which are inside the domain. The red points indicate quadrature points for the domain, the green are for the outside area. b) Reconstruction of a multilayer sphere model. Accurate depiction of the curvature of the sphere is achieved while maintaining a low fundamental mesh resolution.

In total, CutFEM features several differences compared to standard CG-FEM.

- Using the level-set function directly allows for a very accurate representation of the head geometry.
- No possibly complicated mesh generation as in the tetrahedral case is necessary. Misshapen cut-cells are taken care of through Ghost-penalties.
- Ansatzfunctions are defined on the fundamental mesh. This can be chosen coarser than a CG-mesh while maintaining a similar level of accuracy. Thus the number of Degrees of Freedom (i.e. number of Ansatzfunctions) is smaller.
- Most mesh-generators cannot deal with holes in the compartments, which occur for example in the CSF when brain and skull touch.
- A possible downside is the dependence on the penalty parameters γ, γ_G which can strongly influence the result as will be seen in the evaluations.

Having set-up the framework for numerical calculations involving continuous Galerkin and CutFEM methods, we can now proceed comparing them regarding stability and convergence properties.

5. Error Estimation

When giving a priori error estimates of the form

$$||u - u_h|| \leq Ch^s |u|_{H^2}$$

for some $s > 0$ it is usually required that the solution u is in $H^2(\Omega)$ and that the injected current I/primary potential J^p are in $L^2(\partial\Omega)$ or$L^2(\Omega)$ respectively. These requirements are usually not met due to the singularities in the respective terms. Still, the estimates give an idea of how the methods behave under "nice" circumstances. When using the subtraction approach([WKM$^+$07]) to model the primary source term, it can be shown that the error increases as the sources get closer to the next conductivity jump, an effect that has also been shown in numerical studies of other source models for which no error estimate of the kind exists ([PVW16]). As CG- and Cut-FEM differ regarding bilinearforms and FEM-spaces employed, they will be treated individually. The starting point is the same however. Rather than determining an $u \in V$ such that

$$a(u, v) = l(v) \; \forall \; v \in V \tag{5.1}$$

an approximation $u_h \in V_h$ is searched such that

$$\hat{a}(u_h, v_h) = l(v_h) \; \forall \; v_h \in V_h \tag{5.2}$$

for some FEM-space V_h and a bilinearform $\hat{a}$ that may differ from a. The first question that arises is whether solving this auxiliary problem is even related to solving the original one.

5.1. CG-FEM

In CG-FEM we have $V_h \subseteq V$ (meaning its a conforming method) and $\hat{a} = a$. We first note that

$$a(u, v_h) = l(v_h) = a(u_h, v_h) \; \forall \; v_h \in V_h$$

since V_h is a subspace of V. Substracting right from left side and the bilinearity of a then yield the Galerkin Orthogonality

$$a(u - u_h, v_h) = 0 \; \forall \; v_h \in V_h. \tag{5.3}$$

Using this property we can continue estimating the difference between u and u_h. Recalling the coercivity of a one obtains

$$||u - u_h||^2 \leq \frac{1}{\alpha} a(u - u_h, u - u_h)$$

$$= \frac{1}{\alpha}a(u-u_h, u-v_h+v_h-u_h) = \frac{1}{\alpha}a(u-u_h, u-v_h) + \frac{1}{\alpha}a(u-u_h, v_h-u_h)$$

using an arbitrary v_h from V_h and the bilinearity of a. Note that $v_h - u_h \in V_h$, thus the second term is equal to zero. Now recall that a is continuous and thus

$$\frac{1}{\alpha}a(u-u_h, u-v_h) \leq \frac{C}{\alpha}||u-u_h||||u-v_h||.$$

This is true for any $v_h \in V_h$, thus the inequality also holds for the infimum over the v_h. Dividing both sides by $||u-u_h||$ we arrive at

$$||u-u_h|| \leq \inf_{v_h \in V_h} \frac{C}{\alpha}||u-v_h||. \tag{5.4}$$

The coercivity and continuity constants α, C are the same as in Lemma 3.1. This result is known as Céa's Lemma ([Bra07]). It states that the error is proportional to the best possible approximation of u that can be achieved using functions from V_h, it is therefore quasi-optimal. The choice of the FEM-space is thus of tantamount importance. Hence, the next steps will explore the quality of this best possible approximation.

The Bramble-Hilbert Lemma can be used to show that u can be interpolated in V_h on a reference element, also giving an error estimate. Every mesh element is merely a transformation of the reference element, thus the error estimate can also be translated yielding a result for the entire mesh.

Theorem 5.1 (Mesh Interpolation Error using Bramble-Hilbert) *Let $\mathcal{T}_h$ be a triangulation of Ω with vertices $x_1, ..., x_N$, $u \in H^2(\Omega)$, $I_h : H^2 \to V_h$ a linear Interpolation operator such that $I_h u(x_i) = u(x_i)$ for $i = 1, ..., N$. Then there is a $c_\mathcal{T} > 0$ such that*

$$||u - I_h u||_{H^1(\Omega)} \leq c_\mathcal{T} h |u|_{H^2(\Omega)}. \tag{5.5}$$

Proof: see [Bra07] □

Note that the constant $c_\mathcal{T}$ depends strongly on the shape and amount of distortion of the mesh elements. Different measurements exist to determine what constitutes a "good" element, be it minimum or maximum face angle conditions or the size of the largest sphere that can be inscribed into the mesh. In [She02] it is suggested that very "stump" tetrahedrons lead to large errors in the gradient of $u - u_h$. A 2D intuition for this can be seen in Figure 5.1..

Since $I_h u \in V_h$ we can use the result from theorem 5.1 to proceed with equation (5.4), yielding

$$||u-u_h||_{H^1(\Omega)} \leq \inf_{v_h \in V_h} \frac{C}{\alpha}||u-v_h|| \leq \frac{C}{\alpha}||u-I_h u||_{H^1(\Omega)} \leq \frac{C}{\alpha} c_\mathcal{T} h |u|_{H^2(\Omega)}. \tag{5.6}$$

As an extension of this, the Aubin-Nitsche Lemma can be used to give a stronger result for the L^2 error.

$$||u-u_h||_{L^2(\Omega)} \leq \frac{C}{\alpha} c_\mathcal{T} h^2 |u|_{H^2(\Omega)} \tag{5.7}$$

It will be covered more extensively in the CutFEM section.

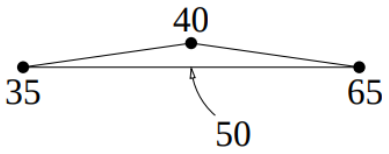

Fig. 5.1.: Effect of stump triangles on Interpolation Error. A function u with vertex values 35, 40, 65 is approximated by a linear interpolation $I_h u$. The interpolation is exact on the vertices, linearity implies that the value on the middle of the line from bottom left to right vertex is 50. If the top vertex moves close to this middle point, the vertical component of the gradient of the Interpolation has to explode to maintain the value of 40 at the top vertex. Thus, "stump" triangles may lead to a massive increase of $||\nabla(u - I_h u)||$ ([She02]).

5.2. CutFEM

In this section we will determine under which conditions the optimal convergence rates of (5.6) and (5.7) can be achieved using CutFEM. The following statements are based on [BH12], [HH02] and [Sch17].

We first check if a solution u to the strong CutFEM formulation (4.9-12) also solves the weak equation (4.23). Equations (4.11) and (4.12) yield that the (non-)symmetry term is zero and the flux term jump-free, thus

$$a(u, v_h) + a^N(u, v_h) + a^G(u, v_h) = \sum_i \int_{\Omega_i} \sigma \nabla u \nabla v_h dx - \int_\Gamma \sigma \nabla u [\![v_h]\!] dS + a^G(u, v_h)$$

$$\overset{part.Int.}{=} -\sum_i \int_{\Omega_i} \nabla\sigma\nabla u v_h dx + \int_\Gamma \sigma \nabla u [\![v_h]\!] dS + \int_{\partial\Omega} \sigma \nabla u v_h dS - \int_\Gamma \sigma \nabla u [\![v_h]\!] dS + a^G(u, v_h)$$

$$= l(v_h) + a^G(u, v_h).$$

The CutFEM approach is thus consistent up to the Ghost-penalty parameter and a modified Galerkin Orthogonality

$$a(u - u_h, v_h) + a^N(u - u_h, v_h) = a^G(u_h, v_h) \tag{5.8}$$

holds for solutions u, u_h to classical and weak formulation respectively.

Central to all following results is the coercivity of the bilinearforms. To prove it, mesh-dependent norms

$$||v||^2_{\pm\frac{1}{2},h,\Gamma} := \sum_{E\in\mathcal{T}_h} \hat{h}^{\mp 1} ||v||^2_{L^2(\Gamma)} \tag{5.9}$$

are introduced. By the Cauchy-Schwarz Inequality

$$\langle u, v\rangle_\Gamma = \int_\Gamma uv dS = \sum_{E\in\mathcal{T}_h} \int_{\Gamma\cap E} \hat{h}^{\frac{1}{2}} u \hat{h}^{-\frac{1}{2}} v dS$$

$$\leq \sum_{E\in\mathcal{T}_h} ||\hat{h}^{\frac{1}{2}} u||^2_{L^2(\Gamma\cap E)} ||\hat{h}^{-\frac{1}{2}} v||^2_{L^2(\Gamma\cap E)} \leq ||u||_{-\frac{1}{2},h,\Gamma} ||v||_{\frac{1}{2},h,\Gamma} \tag{5.10}$$

can be obtained. Next an energy-type norm in which coercivity can be shown is defined as

$$|||v|||^2 := \sum_i ||\nabla v||^2_{L^2(\mathcal{T}_h^i)} + ||[\![v]\!]||^2_{\frac{1}{2},h,\Gamma}. \tag{5.11}$$

The Poincaré Inequality ensures that this is actually a norm. It includes the submesh overlap of the $\mathcal{T}_h^i$ and thus includes the parts of the Ansatzfunctions that would otherwise be cut-off. Not considering those parts could otherwise lead to a deterioration of the system matrix conditioning ([Bur10]). However, the norm over the physical domain ($\cup_i \Omega_i$) alone is not enough to control the gradient of v over the cut-off parts. This can be alleviated using the Ghost-penalty term as can be seen from the following Lemma.

Lemma 5.1 *For all $v \in V_h$ the inequality*

$$\sum_i ||\nabla v||^2_{L^2(\mathcal{T}_h^i)} \leq C_G(||\nabla v||^2_{L^2(\cup\Omega_i)} + a^G(v,v)) \tag{5.12}$$

holds.

Proof: Let $\mathcal{G}_h$ denote the set of elements cut by the level-set and note that the Ansatzfunctions we are looking at are linear on each element, we therefore focus on the case that v is as well. The gradient is thus constant on each element $E \in \mathcal{G}_h$ and can be expressed via the gradient of neighboring hexahedrons $E_i \notin \mathcal{G}_h$ combined with the jump of v on the interface between them.

$$\nabla v|_E = \sum_i (\nabla v|_{E_i} + [\![v]\!]_{EE_i})$$

Having completely uniform hexahedrons leads to

$$||\nabla v||^2_{L^2(E)} \leq \sum_i (||\nabla v||^2_{L^2(E_i)} + ||[\![v]\!]||^2_{L^2(E\cap E_i)}).$$

When summing over all cut-cells we obtain an estimate that includes duplicates of the E_i. However each E_i is connected at most to 8 cut-cells, yielding

$$||\nabla v||^2_{L^2(\mathcal{G}_h)} \leq 8(||\nabla v||^2_{L^2(\cup\Omega_i)} + ||[\![v]\!]||^2_{L^2(\hat{\Gamma})}).$$

In total

$$\sum_i ||\nabla v||^2_{L^2(\mathcal{T}_h^i)} \leq ||\nabla v||^2_{L^2(\mathcal{G}_h)} + ||\nabla v||^2_{L^2(\cup\Omega_i)}$$

$$\leq 9(||\nabla v||^2_{L^2(\cup\Omega_i)} + ||[\![v]\!]||^2_{L^2(\hat{\Gamma})}) \leq 9C_\sigma(||\nabla v||^2_{L^2(\cup\Omega_i)} + a^G(v,v)).$$

□

Coercivity for the symmetric and non-symmetric case can now be shown separately.

Lemma 5.2 (Coercivity)

$$a(v,v) + a^N_{n/s}(v,v) + a^G(v,v) \geq C|||v|||^2$$

for both symmetric and non-symmetric a^N.

Proof: First the non-symmetric case:

$$a(v,v)+a_n^N(v,v)=\sum_i\int_{\Omega_i}\sigma\nabla v\nabla v dx-\int_\Gamma\{\sigma\nabla v\}[\![v]\!]dS+\int_\Gamma\{\sigma\nabla v\}[\![v]\!]dS+\gamma\nu_k\int_\Gamma\frac{\hat\sigma}{\hat h}[\![v]\!]^2dS$$

$$=\sum_i\int_{\Omega_i}\sigma\nabla v\nabla v dx+\gamma\nu_k\int_\Gamma\frac{\hat\sigma}{\hat h}[\![v]\!]^2dS\geq C_\sigma||\nabla v||^2_{L^2(\cup\Omega_i)}+\gamma\nu_k C_\sigma|||[\![v]\!]|||^2_{\frac12,h,\Gamma}$$

$$\overset{5.12}{\geq} C_\sigma C_G^{-1}(\sum_i||\nabla v||^2_{L^2(\mathcal{T}_h^i)}-a^G(v,v))+\gamma\nu_k C_\sigma|||[\![v]\!]|||^2_{\frac12,h,\Gamma}$$

$$\geq C_\sigma\min\{C_G^{-1},\gamma\nu_k\}|||v|||^2-C_G^{-1}a^G(v,v),$$

where $C_\sigma=\min_\Omega\{\sigma,\hat\sigma\}$. The non-symmetric interior penalty Galerkin is thus coercive for any $\gamma>0$. This will change when looking at the symmetric case. Taking the same steps as above yields

$$a(v,v)+a_s^N(v,v)=\sum_i\int_{\Omega_i}\sigma\nabla v\nabla v dx-2\int_\Gamma\{\sigma\nabla v\}[\![v]\!]dS+\gamma\nu_k\int_\Gamma\frac{\hat\sigma}{\hat h}[\![v]\!]^2dS$$

$$\geq C_\sigma C_G^{-1}(\sum_i||\nabla v||^2_{L^2(\mathcal{T}_h^i)}-a^G(v,v))+\gamma\nu_k C_\sigma|||[\![v]\!]|||^2_{\frac12,h,\Gamma}-2\int_\Gamma\{\sigma\nabla v\}[\![v]\!]dS. \tag{5.13}$$

In order to treat the last term separately, a trace inequality

$$||\{\nabla v\}||^2_{-\frac12,h,\Gamma}\leq C_T\sum_i||\nabla v||^2_{L^2(\mathcal{T}_h^i)} \tag{5.14}$$

is needed. To prove it first note that

$$||\{\nabla v\}||^2_{-\frac12,h,\Gamma}=\sum_{E\in\mathcal{T}_h}\hat h||\omega_{\Omega_i}\nabla v^i+\omega_{\Omega_j}\nabla v^j||_{L^2(\Gamma\cap E)}$$

$$\leq\sum_{E\in\mathcal{T}_h}\hat h||\omega_{\Omega_i}\nabla v^i||_{L^2(\Gamma\cap E)}+\hat h||\omega_{\Omega_j}\nabla v^j||_{L^2(\Gamma\cap E)}.$$

Looking at each term individually and using the fact that v^i is linear on Γ and $E\cap\Omega_i$ (the gradient is thus constant) we obtain

$$\hat h\omega_{\Omega_i}||\nabla v||_{L^2(\Gamma\cap E)}=\hat h\omega_{\Omega_i}c_{v^i}|\Gamma\cap E|=\hat h\omega_{\Omega_i}c_{v^i}\frac{|\Gamma\cap E|}{|E\cap\Omega_i|}|E\cap\Omega_i|$$

$$=\omega_{\Omega_i}c_{v^i}\frac{\min\{|E\cap\Omega_i|,|E\cap\Omega_j|\}}{|\Gamma\cap E|}\frac{|\Gamma\cap E|}{|E\cap\Omega_i|}|E\cap\Omega_i|=\omega_{\Omega_i}c_{v^i}\min\{1,\frac{|E\cap\Omega_j|}{|E\cap\Omega_i|}\}|E\cap\Omega_i|$$

$$\leq\omega_{\Omega_i}C_{E_i}||\nabla v||_{L^2(E\cap\Omega_i)}.$$

In the second step the definition of $\hat h$ was used. Note that the constant C_{E_i} depends strongly on how Γ cuts the mesh and thus varies for every element. Returing to the sum we get

$$||\{\nabla v\}||^2_{\frac12,h,\Gamma}\leq\sum_i\sum_{E\in\mathcal{T}_h^i}\max\{\omega_{\Omega_i}C_{E_i},\omega_{\Omega_j}C_{E_j}\}||\nabla v|_{L^2(E)}\leq C_T\sum_i||\nabla v||^2_{L^2(\mathcal{T}_h^i)}$$

which concludes proving the inequality. We can now proceed with the last term from (5.9). First the inequality from (5.7) is used:

$$-2\int_\Gamma \{\sigma\nabla v\}[\![v]\!]dS \geq -2C_\sigma ||\{\nabla v\}||_{-\frac{1}{2},h,\Gamma} |||[\![v]\!]|||_{\frac{1}{2},h,\Gamma}$$

$$\overset{2ab\leq \frac{a^2}{\epsilon}+\epsilon b^2}{\geq} -\frac{1}{\epsilon}C_\sigma^2 ||\{\nabla v\}||^2_{-\frac{1}{2},h,\Gamma} - \epsilon |||[\![v]\!]|||^2_{\frac{1}{2},h,\Gamma}$$

$$\overset{(5.10)}{\geq} -\frac{1}{\epsilon}C_\sigma^2 C_T \sum_i ||\nabla v||^2_{L^2(\mathcal{T}_h^i)} - \epsilon |||[\![v]\!]|||^2_{\frac{1}{2},h,\Gamma}.$$

This estimate holds for any $\epsilon > 0$. Continuing with (5.9) yields

$$a(v,v) + a_s^N(v,v) \geq C_\sigma C_G^{-1}(\sum_i ||\nabla v||^2_{L^2(\mathcal{T}_h^i)} - a^G(v,v)) + \gamma\nu_k C_\sigma |||[\![v]\!]|||^2_{\frac{1}{2},h,\Gamma}$$

$$-\frac{1}{\epsilon}C_\sigma^2 C_T \sum_i ||\nabla v||^2_{L^2(\mathcal{T}_h^i)} - \epsilon |||[\![v]\!]|||^2_{\frac{1}{2},h,\Gamma}$$

$$= (C_\sigma C_G^{-1} - \frac{C_\sigma^2 C_T}{\epsilon}) \sum_i ||\nabla v||^2_{L^2(\mathcal{T}_h^i)} + (\gamma\nu_k C_\sigma - \epsilon) |||[\![v]\!]|||^2_{\frac{1}{2},h,\Gamma} - \frac{1}{\epsilon} C_\sigma C_G^{-1} a^G(v,v)$$

$$\geq \min\{C_\sigma C_G^{-1} - \frac{C_\sigma^2 C_T}{\epsilon}, \gamma\nu_k C_\sigma - \epsilon\} |||v|||^2 - C_G^{-1} a^G(v,v). \tag{5.15}$$

For coercivity the minimum needs to be larger larger than zero, thus we need $\epsilon > C_\sigma C_T C_G$ and $\gamma \geq \frac{\epsilon}{C_\sigma \nu_k}$. This shows that the symmetric penalty Galerkin approach is only coercive if the penalty parameter γ is chosen large enough. As C_T depends largely on the mesh intersection of the level-set functions, so does the required size of γ. □

The continuity of $a(u,v) + a^N_{n/s}(u,v) + a^G(v,v)$ can be shown using the Cauchy-Schwarz inequality combined with steps similar to the ones above.

Coercivity and continuity are necessary to give an a-priori error estimate. A solution u to the classical problem (4.9-12.) however is only defined on the physical domain $\cup_i \Omega_i$, not on the cut-off parts of the submeshes. To measure the error we thus need a norm that is restricted to the pyhsical domain.

$$|||v|||^2_\Omega := ||\nabla v||^2_{L^2(\cup\Omega_i)} + |||[\![v]\!]|||^2_{\frac{1}{2},h,\Gamma} \tag{5.16}$$

It immediately follows that

$$|||v|||_\Omega \leq |||v||| \tag{5.17}$$

for $v \in V_h$. Next, an interpolation operator similar to the one from equation (5.5) in CG-FEM is needed.

Lemma 5.3 *Let $u \in H^2(\Omega)$ and denote by $I^* : H^1(\Omega) \to V_h$ the Clément Interpolation operator. Then*

$$|||u - I^*u|||_\Omega + a^G(I^*u, I^*u)^{\frac{1}{2}} \leq Ch|u|_{H^2(\Omega)}. \tag{5.18}$$

Proof: See [BH12] □

This estimate will be useful when proving optimal convergence rates of the kind

$$|||u - u_h|||_\Omega \leq Ch|u|_{H^2(\Omega)}$$

for solutions u, u_h to the classical and discrete problem respectively. Before proving an estimate like that notice that

$$|||u - u_h|||_\Omega = |||u - I^*u + I^*u - u_h|||_\Omega \leq |||u - I^*u|||_\Omega + |||I^*u - u_h|||. \tag{5.19}$$

We thus first need to gauge the difference between discret solution and the interpolation of the classical one.

Lemma 5.4 *Let u be a solution to (4.9-12), u_h a solution to (4.23) and I^* the Clément Interpolation operator. Then*

$$|||I^*u - u_h||| \leq C(|||u - I^*u|||_\Omega + a^G(I^*u, I^*u)^{\frac{1}{2}}). \tag{5.20}$$

Proof: Let $A(v, w) := a(v, w) + a^N_{n/s}(v, w)$ and $e_h = u_h - I^*u$ (symmetric or non-symmetric makes no difference as long as coercivity is given). Then by the coercivity from Lemma 5.2 we have

$$\begin{aligned}|||e_h|||^2 \leq C(A(e_h, e_h) + a^G(e_h, e_h)) &= A(u_h - u + u - I^*u, e_h) + a^G(e_h, e_h) \\ &= C(A(u_h - u, e_h) + A(u - I^*u, e_h) + a^G(e_h, e_h)).\end{aligned}$$

As $e_h \in V_h$ the Galerkin orthogonality from (5.8) can be used to obtain

$$|||e_h|||^2 \leq C(A(u - I^*u, e_h) - a^G(u_h, e_h) + a^G(e_h, e_h) = A(u - I^*u, e_h) - a^G(I^*u, e_h)).$$

As A and a^G are continuous we get

$$A(u - I^*u, e_h) \leq C|||u - I^*u|||_\Omega |||e_h|||$$

for A and from a Cauchy-Schwarz-type inequality

$$-a^G(I^*u, u_h - I^*u) \leq a^G(I^*u, I^*u)^{\frac{1}{2}} a^G(e_h, e_h)^{\frac{1}{2}} \leq a^G(I^*u, I^*u)^{\frac{1}{2}} |||e_h|||.$$

Combining the two yields

$$\begin{aligned}|||e_h|||^2 \leq C(|||u - I^*u|||_\Omega |||e_h||| + a^G(I^*u, I^*u)^{\frac{1}{2}} |||e_h|||) \\ = C|||e_h|||(|||I^*u - u|||_\Omega + a^G(I^*u, I^*u)^{\frac{1}{2}}).\end{aligned}$$

□

Now the necessary preparations for the a-priori error estimate are made, leading to the following theorem.

Theorem 5.2 (A-priori Error Estimates in Energy and L^2 norm) *Let u be a solution to (4.9-12), u_h a solution to (4.23). Then the following estimate holds for both symmetric and non-symmetric interior penalty Galerkin method*

$$|||u - u_h|||_\Omega \leq Ch|u|_{H^2}. \tag{5.21}$$

Furthermore, for the symmetric version it holds that

$$||u - u_h||_{L^2(\Omega)} \leq Ch^2|u|_{H^2}. \tag{5.22}$$

Proof: For the first inequality we start by applying Lemma 5.4 to equation (5.19) and using the Interpolation estimate from Lemma 5.3 yields

$$\begin{aligned}|||u-u_h|||_\Omega &\leq |||u-I^*u|||_\Omega + C(|||u-I^*u|||_\Omega + a^G(I^*u,I^*u)^{\frac{1}{2}}) \\ &\leq \hat{C}h|u|_{H^2(\Omega)},\end{aligned}$$

thus proving the first estimate. To show the stronger L^2 result from (5.7) for CutFEM, Nitsche's duality trick is applied. Let z be the solution of the adjoint problem

$$\nabla\sigma\nabla z = u-u_h, \quad \text{in } \underset{i}{\cup}\Omega_i \tag{5.23}$$

$$\langle\sigma\nabla z, n\rangle = 0, \quad \text{on } \partial\Omega \tag{5.24}$$

$$[\![z]\!] = 0, \quad \text{on } \Gamma \tag{5.25}$$

$$[\![\sigma\nabla z]\!] = 0, \quad \text{on } \Gamma \tag{5.26}$$

with u, u_h as before. It is assumed that $z \in H^2(\cup\Omega_i)\cup H_0^1(\Omega)$. Then by the same arguments as leading to the Galerkin Orthogonality in (5.9) and using the symmetric penalty term we have

$$a(z,v_h) + a_s^N(z,v_h) = \int_{\cup\Omega_i}(u-u_h)v_h dx \;\forall\; v_h \in V_h. \tag{5.27}$$

Using the symmetry on left hand side and the testfunction $u-u_h$ one obtains

$$a(u-u_h,z) + a_s^N(u-u_h,z) = \int_{\cup\Omega_i}(u-u_h)^2 dx = ||u-u_h||_{L^2(\cup\Omega_i)}. \tag{5.28}$$

This adjoint consistency of the symmetric approach now allows for a stronger error estimate. The non-symmetric version, while maintaining the Galerkin type orthogonality, fails here as for a testfunction v

$$a(v,z) + a_n^N(v,z) = \int_{\cup\Omega_i}(u-u_h)v dx + 2\int_\Gamma\{\sigma\nabla z\}[\![v]\!]dS.$$

This version is thus adjoint-inconsistent.

Proceeding with the left side of (5.27) and using again the abbreviation $A(u,v) = a(u,v) + a_s^N(u,v)$ we again employ the Galerkin orthogonality

$$A(u-u_h,z) = A(u-u_h, z+I^*z-I^*z) \overset{5.9}{=} A(u-u_h, z-I^*z) - a^G(u_h, I^*z). \tag{5.29}$$

Both terms will now be treated separately. For the first, the continuity of A yields

$$A(u-u_h, z-I^*z) \leq |||u-u_h|||_\Omega |||z-I^*z|||_\Omega \leq Ch^2|u|_{H^2(\Omega)}|z|_{H^2(\Omega)}. \tag{5.30}$$

In the second step, the inequalities from (5.18) and the a-priori result from Theorem 5.2 were used. The second term can be approached by reusing the Cauchy-Schwarz type inequality from Lemma 5.4 to obtain

$$-a^G(u_h, I^*z) \leq a^G(u_h,u_h)^{\frac{1}{2}} a^G(I^*z, I^*z)^{\frac{1}{2}}. \tag{5.31}$$

Galerkin Orthogonality and the continuity of A result in

$$a^G(u_h, u_h) = (A(u - u_h, u_h)) = (A(u - u_h, u_h - I^*u) + A(u - u_h, I^*u)$$

$$\leq |||u - u_h|||_\Omega |||u_h - I^*u|||_\Omega + a^G(I^*u, I^*u) \overset{5.19}{\leq} |||u_h - I^*u|||^2_\Omega + a^G(I^*u, I^*u)).$$

After considering both terms separately, proceeding with (5.28) now yields

$$A(u - u_h, z) \leq Ch^2|u|_{H^2}|z|_{H^2} + a^G(I^*z, I^*z)^{\frac{1}{2}}(|||u_h - I^*u|||_\Omega + a^G(I^*u, I^*u)^{\frac{1}{2}})$$

$$\overset{5.20}{\leq} Ch^2|u|_{H^2}|z|_{H^2} + a^G(I^*z, I^*z)^{\frac{1}{2}}(|||u - I^*u|||_\Omega + 2a^G(I^*u, I^*u)^{\frac{1}{2}})$$

$$\overset{5.18}{\leq} Ch^2|u|_{H^2}|z|_{H^2} + \hat{C}h^2|z|_{H^2}|u|_{H^2}.$$

To complete the proof note that solution z to the PDE (5.22-25) depends continuously on the input data $u - u_h$ ([CZ98]), i.e.

$$|z|_{H^2} \leq C||u - u_h||_{L^2(\Omega)}. \tag{5.32}$$

Thus, in summary we have

$$||u - u_h||_{L^2(\Omega)} = A(u - u_h, z) \leq Ch^2|u|_{H^2}||u - u_h||_{L^2(\Omega)}$$

which proves the theorem. □

In this chapter the differences and similarities of CG- and CutFEM with regard to convergence behavior and stability were examined. Similar convergence rates for CG- and symmetric CutFEM were found. The upper bound for the non-symmetric CutFEM's convergence rate is worse due to its lack of adjoint consistency. However it has the advantage of being robust with regard to the choice of penalty parameters while the symmetric approach depends on a sufficiently large γ. In summary one could thus expect the non-symmetric version to yield more reliable results while requiring higher mesh resolutions due to the possibly slower convergence.Furthermore the motivation for the choice of the Ghost-penalty term was given. It is a means to control the entirety of the overlapping submeshes rather than only the physical domain itself.

Finally, a reasoning for an error source in the potential's gradient due to deformed mesh tetrahedrons in the CG-FEM was given. Looking forward to numerical experiments one may expect this to be more relevant for tDCS than for EEG as the latter is only interested in the potential value, not in the electric field or current density.

6. Numerical studies

As mentioned in chapter one, the goal of forward modeling in bioelectromagnetism lies in creating a reliable Lead-Field or tDCS matrix to be used for the inverse problem. Doing so requires the usage of an accurate depiction of the head's geometry, i.e. a realistic head-model created from MRI-imaging ([CVWK15]). In the absence of analytical solutions one has to rely on a numerical algorithm for this case. The two methods presented in the previous section are similar with regard to theoretical convergence rate but the CG-FEM might be inferior at modeling scenarios as the one described in the following section.

6.1. Geometries with touching surfaces

When taking MRI-images of the head, the patient usually lies in a supine position inside the machine. This causes the brain that normally floats in the CSF to "sink" to the bottom, touching the skull at the back of the head. The boundary of the CSF thus has a hole at the touching points, a situation that most mesh generators circumvent by adding an artificial layer of CSF in between skull and brain. Furthermore, to represent these very thin parts of CSF, more distorted tetrahedrons may be used, leading to the possible increase in error discussed in the previous section. CutFEM, having barely any restrictions with regard to shape of the compartments, may have an advantage in such a scenario. The goal of this chapter is the creation of a model that approximates such a situation while also featuring analytical solutions for comparison.

6.1.1. Model Setup

The idea is to use a 4 layered spheres, representing scalp, skull, CSF and brain. The three outer ones are concentric while the inner one is shifted to one side by the CSF's thickness (see Figure 6.1.). It thus touches the skull sphere in exactly one point. We then set the same conductivity for CSF and brain implying that this model is identical to a 3-layer concentric sphere model (without CSF) in terms of electrical conduction. Numerical solutions to the 3- and 4-layer models should thus converge to the same solution, which can be computed analytically. For CutFEM, one could then argue that a difference in measured errors would be due to the more intricate way in which the level-set functions cut the mesh, while for CG-FEM it might be due to the less accurate meshing process with artificial CSF and misshapen tetrahedrons.

In [Nüß18] the CutFEM approach was compared to tetrahedral CG-FEM in a concentric sphere scenario for EEG. In this study, 2 mm CutFEM and CG-FEM were compared, CutFEM outperforming the other in 3 out of 4 categories. It is however significantly more time-consuming. Thus, if not stated differently, a tetrahedral model with a resolution of

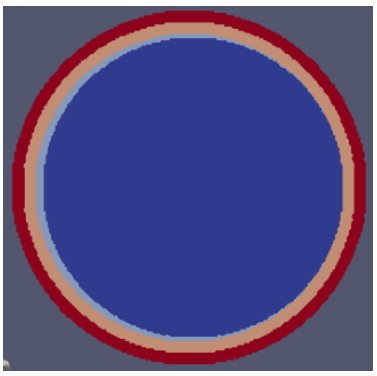

Fig. 6.1.: Depiction of the 4-layer-sphere model used. The layers from red to blue are scalp, skull, CSF and brain. The brain is shifted to the right, thus shares exactly one point with the skull.

around 1 mm will be compared to a CutFEM model with 90 by 90 by 90 fundamental mesh cells or about 2.15 mm resolution, ensuring comparability with regard to computational cost. For the touching sphere model mentioned above, this yields a difference in number of degrees of freedom of a factor of 4.97, CutFEM being on the lower end.

The radii, conductivities and centers of the spheres can be seen in Table 6.2.

	Radius mm	Center	σ S/m
Scalp	92	(127 127 127)	0.33
Skull	86	(127 127 127)	0.01
CSF	80	(127 127 127)	0.33
Brain	78	(129 127 127)	0.33

Table 6.2.: Radii, center and conductivity values for the shifted sphere model. The point where brain and skull touch is at (207 127 127).

As EEG source model, the St. Venant approach (see A.2. for a brief description and the parameters used) will be employed. It outperformed the partial Integration approach in the aforementioned CutFEM study and in a CG study in [BPV$^+$15]. In the latter it also yielded reliable results when compared to other existing models like the H(div)- approach.

200 uniformly distributed electrode sensors are placed on the surface of the scalp sphere. To calculate the Lead-Field matrix for such a large number of sources, a Transfer-Matrix approach (see A.1.) is used. Note that at the time this thesis was written, the approach is only implemented for numerical schemes that feature symmetric stiffness matrices or adjoint consistency. The impact this has on the NWIPG version of CutFEM will be discussed later in the chapter.

Unless stated differently, the source electrode for tDCS is located directly above the point of contact and the sink electrode is placed at the sources antipodal position.

The numerical solutions are computed using the *duneuro*-Toolbox (see [NPS$^+$19] and the implementation chapter). Analytical solutions to the EEG are evaluated using fieldtrip ([OFMS11]) and for tDCS via a python script that was also used in ([Vog19]).

6.1.2. Error Measures

EEG

As the EEG is measured as potential at the scalp electrodes, we are only interested in the errors at those positions. Two different error measures will be employed, the relative difference measure (RDM) and the magnitude error (MAG). By $u^{ana}, u^{num} \in \mathbb{R}^s$ the potential values taken at the electrodes of analytical and numerical solution are denoted. Here s again denotes the number of electrodes.

Definition 6.1 (Relative Difference Measure) *The RDM measures the difference in potential distribution. It is stated in percent and is equal to zero if for any sensor both analytical and numerical solution take up the same proportion of their solution's respective total potential. It is however blind to differences in magnitude.*

$$RDM(u^{ana}, u^{num}) = 50 * ||\frac{u^{ana}}{||u^{ana}||_2} - \frac{u^{num}}{||u^{num}||_2}||_2 \tag{6.1}$$

It ranges from 0 *to* 100*, the optimal value being* 0*.*

Definition 6.2 (Magnitude Error) *The MAG is complementary to the RDM in the sense that it solely measures differences in magnitude while ignoring any distributional differences.*

$$MAG(u^{ana}, u^{num}) = 100 * (\frac{||u^{num}||_2}{||u^{ana}||_2} - 1) \tag{6.2}$$

Measured in percent, its optimal value is 0*. It is unbounded from above and bound by* -100 *from below.*

In the following studies these errors will be measured individually for various source locations. As mentioned in chapter 4, the numerical errors increase when the distance between examined source and the closest conductivity jump decreases. In studies where sources s of various depths are examined, they will thus be grouped by their eccentricity

$$ecc(s) := \frac{||x_s - c_{brain}||_2}{r_{brain}}. \tag{6.3}$$

Here x_s denotes the source location, c_{CSF}, r_{CSF} the center and radius of the CSF sphere respectively. The CSF values are used as the first conductivity jump is at the transition from CSF to skull. In scenarios, where only very eccentric sources near the point of contact of skull and brain are used, this distinction is omitted. The results will also be grouped regarding the orientation of the dipole, it either being radial or tangential with respect to the sphere surface.

tDCS

In tDCS, the electric potential is of secondary interest as the inverse problem maximizes the current density vector J at a target region. Similarly to the EEG, both orientation and magnitude of the vector are examined. The angle between the vectors is stated as

$$A(J^{ana}(x), J^{num}(x)) = acos\langle\frac{J^{ana}(x)}{||J^{ana}(x)||_2} - \frac{J^{num}(x)}{||J^{num}(x)||_2}\rangle, \tag{6.4}$$

where $J^{ana}(x) := -\sigma(x)\nabla u^{ana}(x)$ and J^{num} analogue. The angle is stated in degrees, bounded by 0 and 180. For the magnitude

$$MAG(J^{ana}(x), J^{num}(x)) = 100 * (\frac{J^{num}(x)}{J^{ana}(x)} - 1) \tag{6.5}$$

is used. The magnitudal error is again stated in percent with an optimal value of zero. To calculate the gradient of the analytical potential, a five-point-stencil method

$$\frac{\partial u^{ana}}{\partial x_i}(x) \approx \frac{-u^{ana}(x + 2he_i)) + 8u^{ana}(x + he_i) - 8u^{ana}(x - he_i) + u^{ana}(x - 2he_i)}{12h}$$

with $h = 1e - 5$ is used. The errors may again be grouped by categories, either eccentricity for points inside the brain or the compartment they belong to. The evaluation points will usually be the centerpoints of the tetrahedral or fundamental mesh elements.

Now that the preliminaries have been stated we can proceed with the actual measurements. To properly compare Cut- and CG-FEM first reliable penalty parameters for CutFEM need to be determined.

6.2. Study 1: NWIPG/SWIPG Penalty Parameter Comparison

In the mentioned CutFEM studies in [Nüß18], a Nitsche-penalty $\gamma = 16$ and a ghost-penalty $\gamma_G = 0.005$ were used. These are taken as a starting point to vary the parameters individually. 6 different Nitsche-penalties γ, 10,16,20,40,70,100 and 4 different ghost penalties γ_G, 0.005, 0.05, 0.5, 5 are compared for both symmetric (SWIPG) and non-symmetric (NWIPG) CutFEM in both an EEG and a tDCS environment.

EEG

For the EEG, mostly eccentric sources are examined, therefore 5816 radial and 5749 tangential sources were placed uniformly in an area between 32 and 0.3 mm off the point of contact. Their eccentricities range from 0.91 to 0.99.

The results for varying Nitsche-parameters can be found in Figure 6.3. As mentioned in the previous chapter, SWIPG's coercivity depends on the size of γ. It is thus unsurprising to see that throughout both error measures and both source directions an increase in γ results in a clear reduction in errors. The interquartile range of the RDM for tangential sources decreases from 0.75 at $\gamma = 10$ to 0.10 at $\gamma = 100$, the median from 0.95 to 0.15. The decrement is largest for the lower penalty parameters, after $\gamma = 40$ the gains are only marginal. While the overall errors are fairly low, most sources not exceeding two to three percent, outlier values not visible in the box plots need to be mentioned. The largest ranges from 45.95 for $\gamma = 16$ to 2.06 for $\gamma = 0$. There were 62 outliers with an RDM larger than 15. Their average distance to the point of contact is 6 mm while the average distance over all sources is 17 mm. The outliers thus mainly occur close to the touching point. Similar results are obtained for MAG and for radial sources. The SWIPG method is thus highly responsive to a variation in γ.

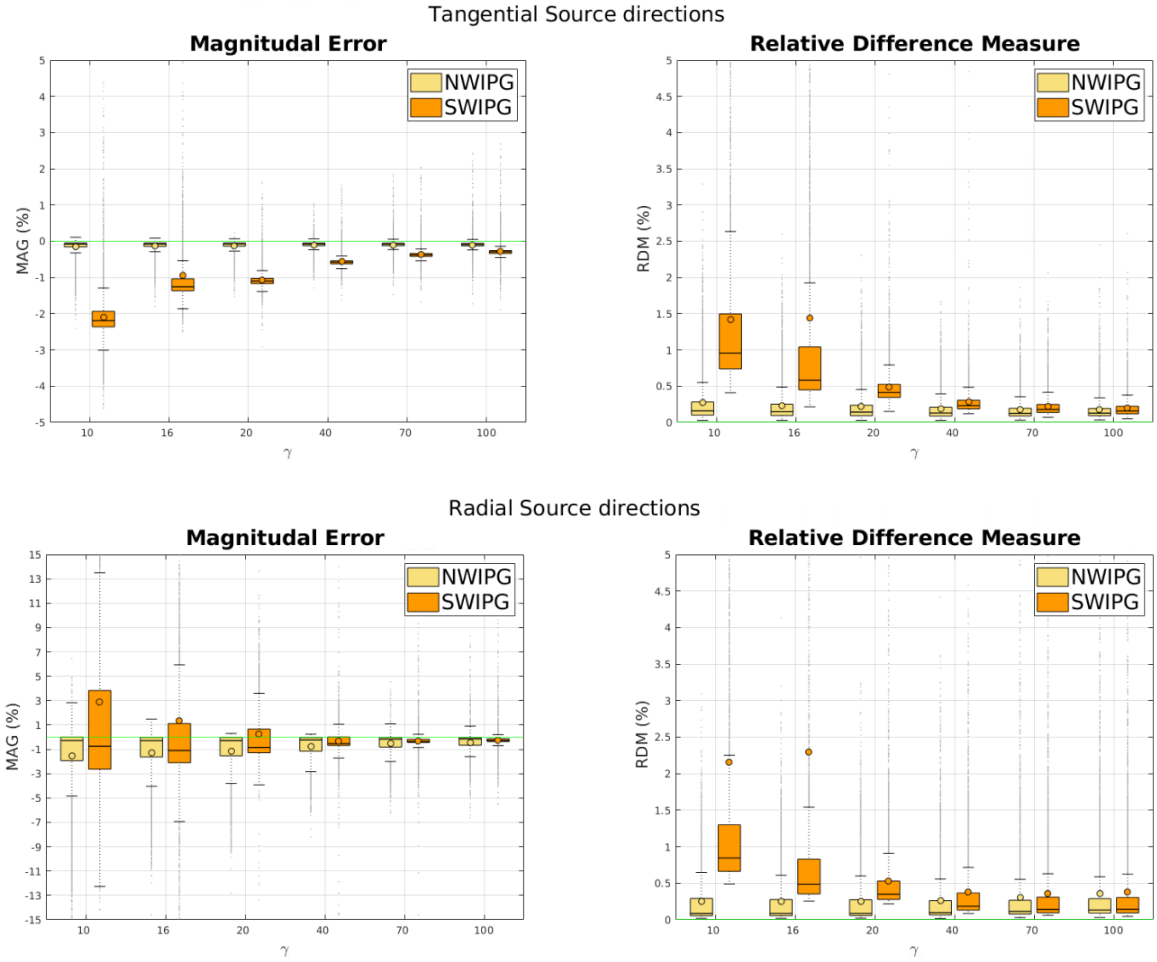

Fig. 6.3.: Overview of different EEG-errors for different Nitsche-penalty parameters. Top: Errors for tangential source directions. Bottom: Errors for radial source directions. Errors are in percent, the green line marks optimal error values. Depicted by the circle is the average error value of each category.

As it is unconditionally coercive, the lower responsiveness of the NWIPG does not come as a surprise. For tangential sources the RDM's interquartile range (IQR) decreases from 0.18 to 0.09 , the highest outlier from 3.28 to 1.66 at $\gamma = 40$. Unexpected however is the fact that the method performs as good or slightly better than SWIPG in almost all categories even at high γ values. Only the MAG error for radial sources for $\gamma \geq 40$ is slightly better for SWIPG. Unexpected, because in the previous chapter a higher convergence rate for the SWIPG for the potential has been shown. Furthermore, as mentioned in the Model Setup section, a Transfer Matrix approach for methods with symmetric stiffness matrices is used. For NWIPG the Transfer Matrix solution is tantamount to the solution of the problem: Find $u_h \in V_h$ such that

$$\hat{a}(v_h, u_h) = l(v_h) \; \forall \; v_h \in V_h.$$

Duneuro also offers a method to directly solve the forward problem for single sources, a comparison of Transfer Matrix and direct computation can be seen in Figure 6.4. As can be seen, the error introduced by NWIPG's ajdoint inconsistency declines rapidly with an

increase in resolution. At 2 mm there is barely any difference between the two. These marginal differences indicate that the NWIPG method is, up to a small error, adjoint consistent regarding the EEG forward problem. As adjoint consistency is the prerequisite for the higher convergence rate of SWIPG, this explains the similar errors of the two methods. For more details on the different convergence behavior, see section 4.2.

mm	2	4	8	16
MAG	0.0013	0.0011	-0.0122	-0.47
RDM	0.0146	0.066	0.3796	1.25

Table 6.4.: Difference between numerical solutions calculated with and without the Transfer-Matrix approach using the NWIPG approach. The direct computation is considered the "analytical" solution in this case. Measures were averaged over 5 random source locations and directions.

To conclude, both SWIPG and NWIPG yield similar results for sufficiently large $\gamma-$values. The NWIPG method however has shown higher consistency throughout the different parameter settings, indicating a higher reliability for scenarios where no large set of parameters can be tested.

The results for the ghost-penalty variation can be found in figure 6.5. Except for the starting point at $\gamma_G = 0.005$ the results for SWIPG and NWIPG are similar. The SWIPG's interquartile range for the tangential source RDM first decreases from 0.59 to 0.23 at $\gamma_G = 0.05$, then increases up to 1.63. Too high a ghost-penalty thus leads to an overall decrease in accuracy. Noticeable is the effect γ_G has on outliers. Starting again at 45.95 their maximum first declines to 5.48 at $\gamma_G = 0.05$ before increasing to 9.47 for the largest ghost-penalty. Thus, even when chosen so large that it noticeably distorts the overall results, it still controls the area surrounding the point of contact. As there are no high outliers in the NWIPG, increasing the ghost-penalty here only lead to the same overall increase in errors measured. It thus appears to be a parameter more relevant to the SWIPG method.

An optimized test with a Nitsche-penalty of 40 and a Ghost-penalty of 0.05 on the right of figure 6.5. emphasizes the relevance of the correct Nitsche-parameter over the optimal Ghost-penalty for SWIPG. The effects on NWIPG are negligible.

Regarding computation cost, the time required to setup the linear equation system (A.2) and to apply the transfer matrices to the source vectors is largely independent of the parameters chosen. The primary difference lies in the number of iterations that the ISTL-solver requires to solve the linear equation system. An overview of the number of iterations needed can be found in Table 6.6. For the SWIPG both choosing too small and too high a Nitsche- or Ghost-penalty results in a significant increase in computation time. The NWIPG method is slightly slower the higher the Nitsche-penalty is chosen while also profiting from choosing a mid-range γ_G. Overall, the computation time of the NWIPG method shows a lower sensitivity to the parameters than SWIPG.

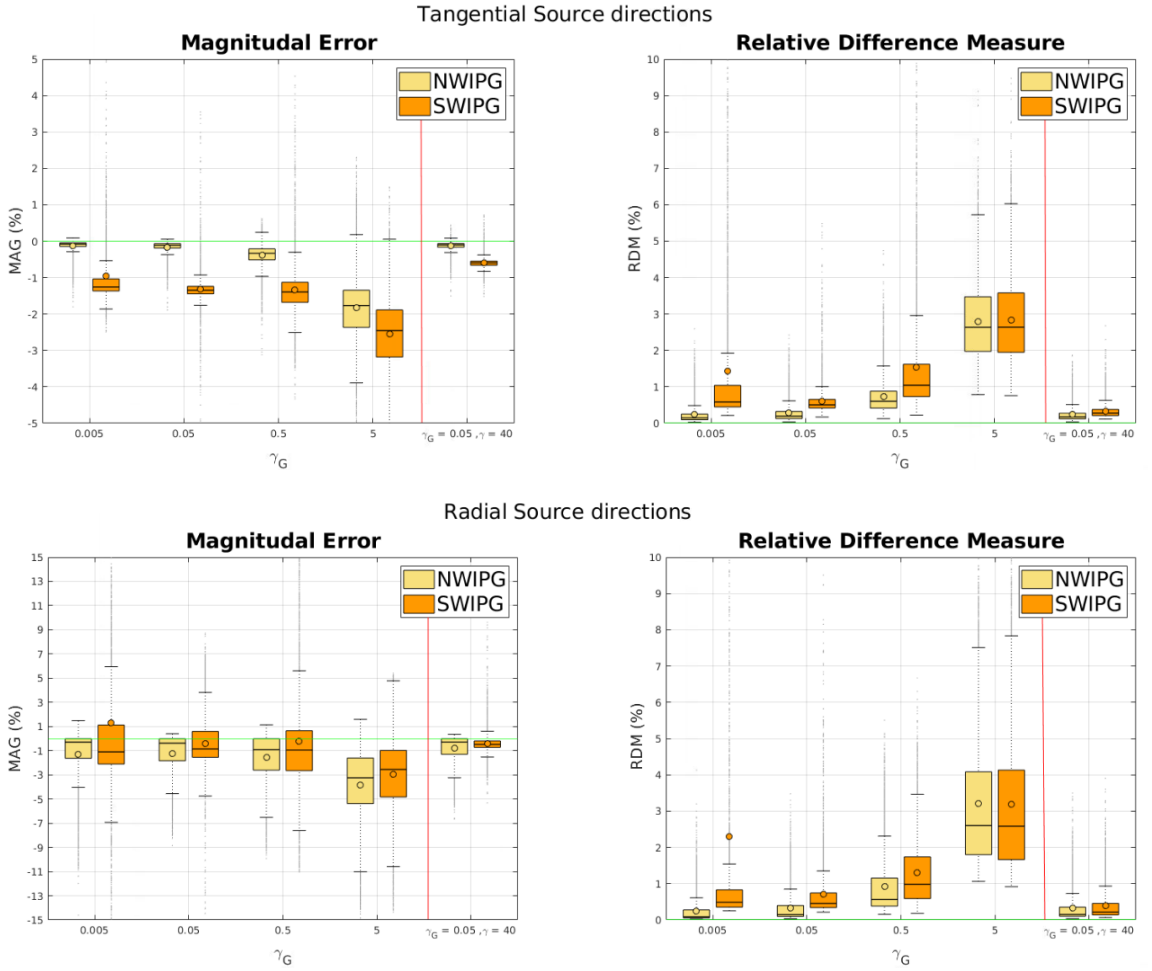

Fig. 6.5.: Overview of different EEG-errors for different Ghost-penalty parameters. Top: Errors for tangential source directions. Bottom: Errors for radial source directions. Errors are in percent, the green line marks optimal error values. Separated by the red line: Errors for NWIPG and SWIPG with the optimal Nitsche-penalty value 40 and ghost penalty 0.05.

γ	10	16	20	40	70	100	γ_G	0.005	0.05	0.5	5
NWIPG	93	112	129	183	238	271		112	97	75	108
SWIPG	480	242	199	221	248	270		242	138	84	104

Table 6.6.: Number of solver iterations needed to compute one column of the Transfer Matrix. On the left: Iterations for the different values of the Nitsche-penalty. Right: Iterations for different Ghost-penalties. One solver iterations corresponds to roughly 1.1 seconds computation time on an i7-6700 CPU with 32GB RAM. For 200 electrodes used, a difference of 100 iterations thus results in a difference of about 6 hours total computation time.

tDCS

For tDCS, the same parameters as for EEG are used again for both NWIPG and SWIPG. Examined are 4888 brain- or CSF-points with an eccentricity greater than 80 and a distance to the point of contact of less than 30 mm. All points are at the center of a fundamental mesh cell. Figure 6.7. shows the findings for a variation of γ. As is immediately apparent, the results for the most part mirror the EEG-findings. For SWIPG, the MAG-IQR decreases from 0.45 to 0.09 with an increase in γ, with only marginal decreases after $\gamma = 40$, from where on NWIPG and SWIPG yield mostly identical results. The same can be said for the vector angle. IQR's for NWIPG remain mostly unchanged, however, it is noteworthy that γ seems to have a strong influence on outliers. The maximal angle difference is 122.23 degrees at $\gamma = 10$ and decreases slowly towards 12.68 degrees at $\gamma = 100$. Similar differences are observed for SWIPG.

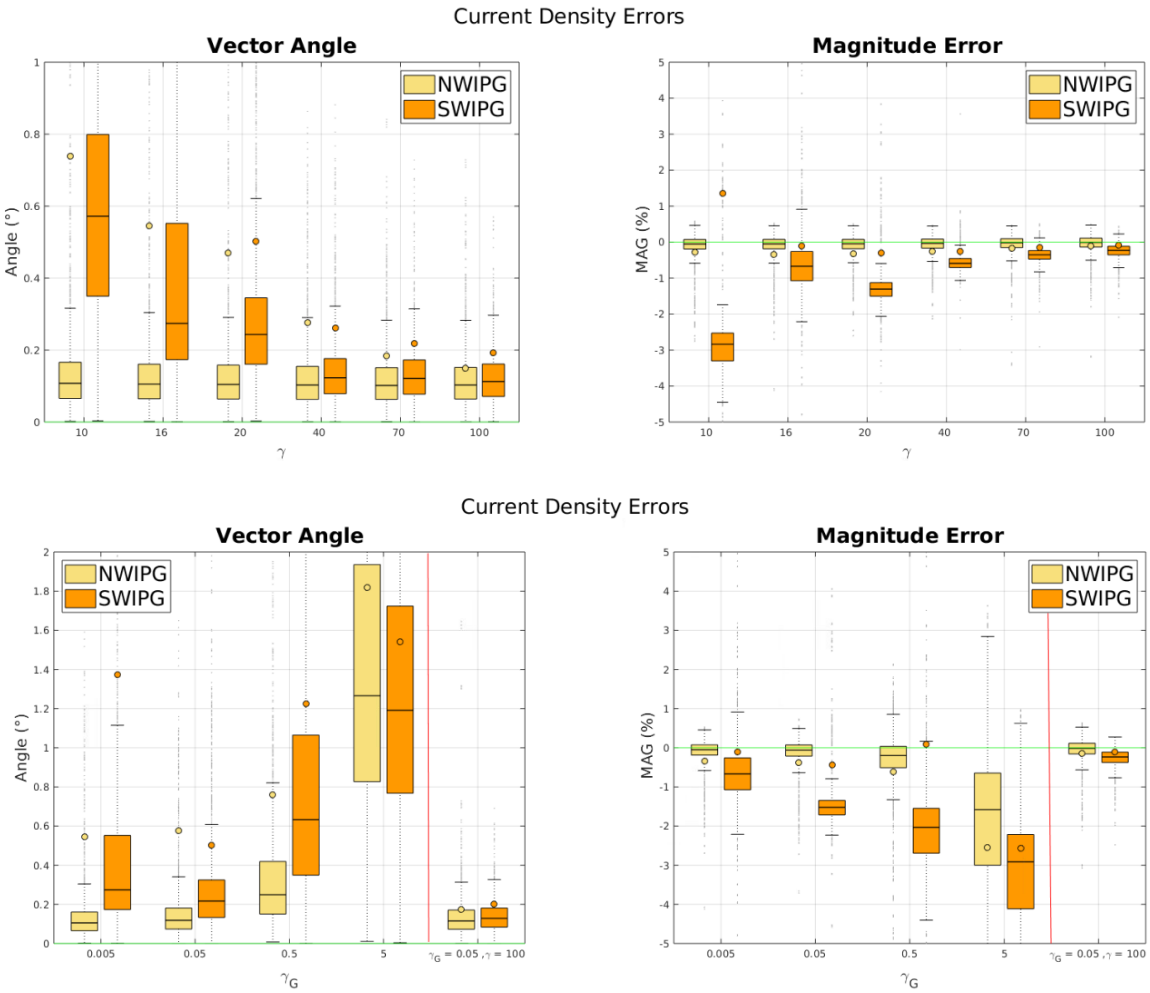

Fig. 6.7.: Overview of tDCS-errors for different Nitsche- and Ghost-penalty parameters. Top: Differences for Nitsche-penalty variation. Bottom: Differences for Ghost-penalties. Separated by the red line: Results for $\gamma = 100$, $\gamma_G = 0.05$. Left: Angles between Vectors in degrees. Right: Vector magnitude differences in percent. The green line marks optimal error values. Depicted by the circle is the average error value of each category.

The findings for Ghost-penalty variations can also be seen in figure 6.7. The results are again similar to the ones in the EEG-section. SWIPG profits from a mid-range γ_G, while NWIPG does not profit at all from an increase in γ_G. Both methods slightly deteriorate when too high a Ghost-penalty is chosen. Choosing a combination of a high γ-value of 100 and a mid-range γ_G of 0.05 resulted in negligible differences to variant with $\gamma_G = 0.005$ from the Nitsche-variation section. In all of the scenarios, eccentricity was more important for error size than proximity to the touching point.

In this study it was found that the SWIPG method strongly relies on choosing the proper penalty parameters, the optimal values being around $\gamma = 40$ and $\gamma_G = 0.05$ for EEG and a Nitsche parameter of 100 for tDCS. Given these, both SWIPG and NWIPG featured very comparable results in the EEG Lead-field computation or current density estimation. NWIPG's slower theoretical convergence rate had no impact on the 2 mm models used and the inaccuracy from using the Transfer-Matrix approach in EEG was also shown to be insignificant. Its high convergence rate and robustness thus make NWIPG the preferable method for the scenario. The more stable computation times only emphasize this.

Having found a CutFEM contestant for a comparison with CG-FEM, the next section is concerned with choosing the proper mesh for the latter.

6.3. Study 2: Element Distortion Effects on CG-FEM

In this study, 2 tetrahedral meshes with about 1 mm resolution are examined with respect to a shape-error correlation. The meshes were created using Gmsh([GR09]) and the Zeffiro user interface for Matlab ([HRP19]). Gmsh uses a Delaunay Triangulation, making sure that for every tetrahedron the circumcircle, the circle through its 4 vertices, does not contain vertices of other elements. It should thus inherently prevent sliver elements. However, brain and skull are separated by a tiny amount of CSF, in the test-case 0.1 mm at what should be the point of contact. This replicates the thin layer of CSF that would otherwise be added in during mesh generation of a realistic head-model. Gmsh also allows for local mesh refinement. To ensure that the compartments are optimally represented, scalp, skull and especially CSF use smaller tetrahedrons than the brain. An overview of the tetrahedrons used in each compartment can be found in table 6.8. A total of 2 611 902 vertices are used, corresponding to the same number of Degrees of Freedom.

Zeffiro on the other hand has no such restrictions. It first takes in a surface triangulation of each compartment. Then it creates a regular hexahedral mesh that is independent of the surface triangulations, much like the fundamental mesh in CutFEM. The third step is to decide for each hexahedron which compartment it belongs to. This is based on the position of the element with regard to the surfaces. Thus, unlike to CutFEM, each hexahedron belongs to one compartment only. The elements are then split into 6 tetrahedrons each. As a last step, laplacian smoothing is used to smooth out the staircase pattern of the hexahedrons. No local mesh refinement is employed, the resolution is a constant 1 mm throughout the mesh, yielding 3 260 808 DoF's. Figure 6.9. shows the area around the point of contact as meshed by Gmsh and Zeffiro in addition to its TPMC reconstruction for CutFEM. Where for Gmsh the 0.1 mm thin layer of CSF is barely visible, but meshed in its entirety, Zeffiro simply ignores the CSF layer. Also the slightly smoothed staircase pattern in Zeffiro is visible. The CSF in the TPMC-version is only visible in fragments.

EEG

Again the focus lies on eccentric sources near the skull/brain touching point. Randomly selecting source points is unfeasible in this situation as Zeffiro inaccurately depicts the sphere surface. Tetrahedrons belonging to the skull compartment were found to reach more than 1 mm into the brain compartment. Randomly choosing a source inside one of those

	#Elements	% total El.	% Vol
Scalp	1,597,282	9.73	18.32
Skull	8,638,424	52.64	15.93
CSF	2,075,210	12.65	4.81
Brain	4,099,386	24.98	60.94

Table 6.8.: Overview of Gmsh's tetrahedron usage in each compartment. From left to right: Total number of elements per compartment, each compartments share of the overall number of elements in the mesh and each compartments share of the models total volume. CSF and skull contain a disproportionate amount of tetrahedrons.

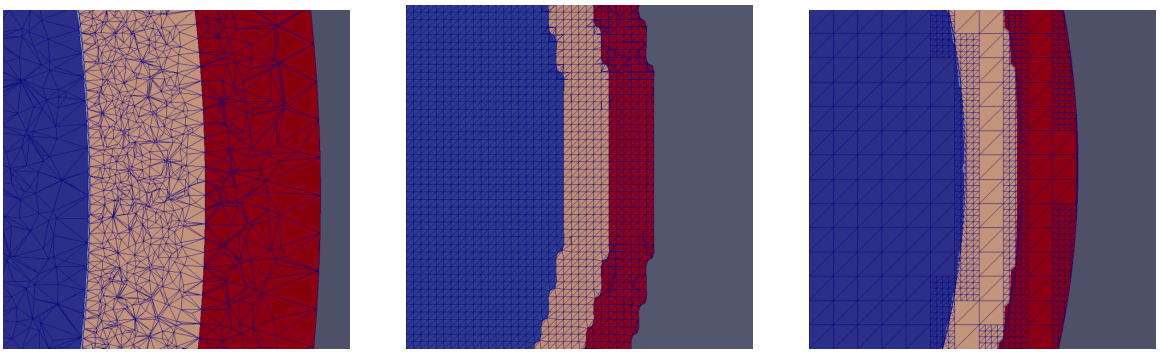

a) Gmsh b) Zeffiro c) TPMC-reconstruction

Fig. 6.9.: Comparison of Gmsh, Zeffiro and the TPMC-algorithm with regard to the reconstruction of the area around the point of contact. Blue portrays the brain, teal (barely visible) the CSF, beige the skull and red the scalp. The black grid indicates the respective mesh.

elements massively distorts the numerical result due to the different conductivity inside. Instead, the centers of 5288 tetrahedrons belonging to the brain compartment were chosen as source points. Their distance to the point of contact was less than 8 mm, eccentricities ranged from 0.903 to 0.989. The resulting radial and tangential errors can be seen in figure 6.10. As is immediately apparent, the mesh created by Gmsh offers significantly better performance in all 4 categories. The interquartile range for tangential sources is lower by a factor of 7.1 and 3.24 for MAG and RDM respectively. Both methods showed no extreme outlier values, the highest (absolut) MAG value is 1.98 for Gmsh and 8.9 for Zeffiro, the highest RDM values are 5.4 and 2.38, yielding similar differences as the IQR.

The lack of outlier values indicates that there might not be a strong correlation between element shape and error magnitude. As a shape measure for the source elements E, the ratio

$$s(E) := \frac{r_{circ}(E)}{r_{insc}(E)}$$

of the radius of the circumscribing circle through all 4 element vertices to the radius of the largest circle that can be fit inside the element is used. A Graph relating $s(E)$ to RDM/MAG for the mesh generated by Gmsh can be found in figure 6.11. As can be seen, while the ratio varies significantly, the error measures do not follow suit. The same can be said for Zeffiro. In particular, all tetrahedrons E that both belong to the brain compartment and less than 8 mm distant from the point of contact had an almost identical shape parameter $s(E)$ between 3.4 and 3.6. The smoothing applied thus did not affect the brain compartment. To better measure the influence of tetrahedron shape on meshes generated by Zeffiro, one would probably have to study meshes with non-spherical brain compartments, i.e. meshes where the deformation is located in the brain and not in the CSF.

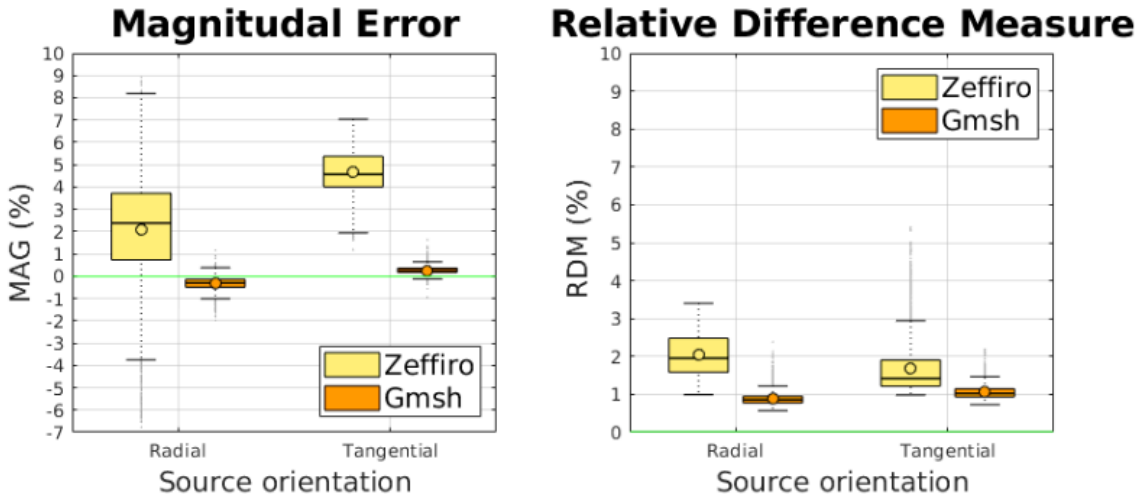

Fig. 6.10.: EEG-comparison of meshes created by Zeffiro and Gmsh. Left: Magnitudal Errors. Right: Relative Difference Measure. Both measures are subdivided by tangential and radial source directions. The circles again depict the averages.

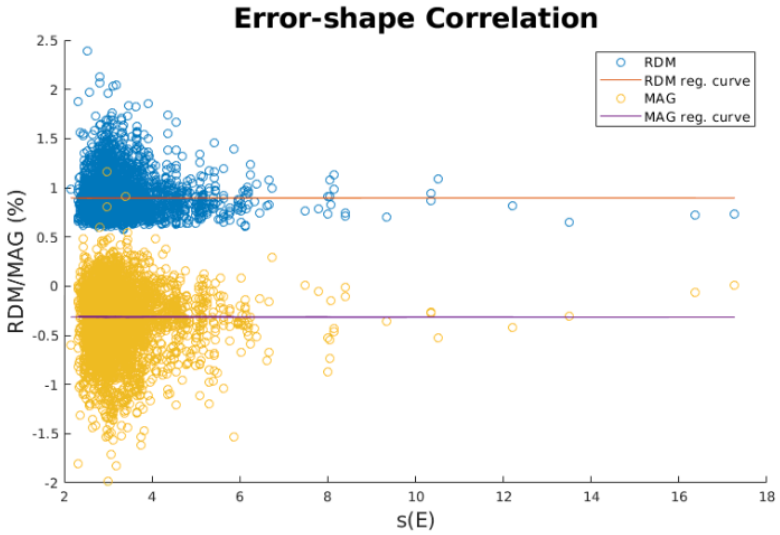

Fig. 6.11.: Shape-Error Correlation for Gmsh. The graph shows the RDM (blue) and MAG (yellow) values against the shape measure of the containing tetrahedrons. The regression curves are a linear fit to the respective data points.

Fig. 6.12.: TDCS-comparison of Gmsh and Zeffiro. Left: Vector angles in degrees. Right: Vector Magnitude differences in percent. The green lines indicate optimal values, the circle depicts the average error per category.

tDCS

For tDCS, the current density inside the Brain/CSF and skull compartment are analyzed. 1512 sample points each were taken, the brain coordinates have an eccentricity greater than 0.975 and a distance to the point of contact of less than 20 mm. The skull points also meet the latter requirement. The results can be seen in figure 6.12. As was already seen in the EEG-comparison, the Zeffiro results massively deteriorate at high eccentricities, with IQR's of 17.99 for the vector angle in the brain/CSF compartment and over 60 for the skull domain. Outliers may range up to 90 and 70 degrees respectively. Gmsh produces much more reliable results with IQR's of 0.93 and 0.46 for brain/CSF and skull angles, and maximal angles of slightly over 9 degrees. Notably the results for the skull compartment are slightly better than for the interior domain, this is in all likelihood due to the more refined meshing in the skull and the fact, that the skull points are located throughout its entire thickness.

The correlation between tetrahedron shape and error size can be seen in figure 6.13. Just like in the EEG-case, misshapen elements did not coincide with large errors. The results for Zeffiro are similar.

In this study the meshes by two different mesh generators were compared. It was found that the mesh generated by Gmsh produced better results for eccentric sources. Both meshes showed no susceptibility to more deformed elements when computing the electric potential or its derivative. For the EEG they both showed overall stable results with regard to outliers. The Zeffiro Interface usually avoids its overall higher EEG-errors at high eccentricities by simply limiting the minimal distance between skull and feasible source space.

Overall, for a Lead-Field or tDCS-Matrix generation, a more involved meshing procedure like the one Gmsh uses appears to be neccessary to obtain reliable results. The arguably more basic Zeffiro algorithm, a tool that focuses on solving the inverse problem rather than Lead-field generation, is insufficient at high eccentricities.

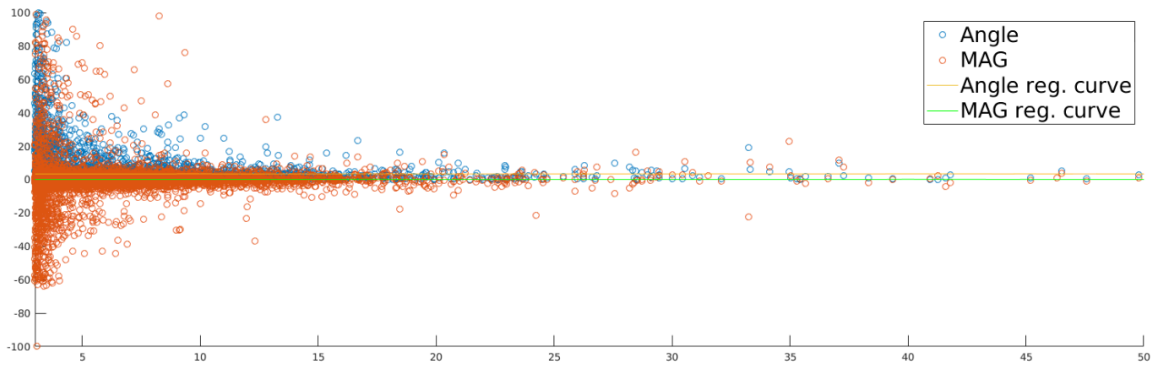

Fig. 6.13.: TDCS-shape-error Correlation for Gmsh. The graph shows the RDM (blue) and MAG (yellow) values against the shape measure of the containing tetrahedrons. The regression curves are a linear fit to the respective data points.

6.4. Study 3: Comparison of Cut- and CG-FEM

Now that both a suitable model for Continuous-Galerkin and Cut finite element method have been selected, we can proceed by comparing the two. Where the previous studies focused primarily on the effects close to the point of contact, this study will look at the model as a whole. A NWIPG approach with Nitsche-penalty 40 and Ghost-penalty 0.05 for Cut-FEM and the same Gmsh created mesh as from the previous study was used for CG-FEM. This includes source and examination locations throughout the entire brain compartment as well as the skull for tDCS. As a further means of comparison, 3-layer concentric sphere models not including CSF were created for both Cut- and CG-FEM. Differences between the shifted 4-layer and the 3-layer models will be a further indicator for the respective method's susceptibility to touching surfaces.

EEG

For the EEG-Comparison, 10 different eccentricities with were selected and radial and tangential orientations computed. The positions are spread evenly throughout the brain compartment, an overview of the eccentricities used and the distribution of sources can be found below.

Ecc.	0.3	0.6	0.7	0.85	0.9	0.93	0.96	0.97	0.98	0.99
# Sources	978	1015	1004	1012	1011	986	994	1053	899	960

A source belonging to an ecc. group indicates it has an eccentricity higher than its group value but lower than the next groups. As the eccentricity is related to distance to the skull, not the CSF, sources with an ecc. larger than 0.97 are all located in the hemisphere containing the point of contact.

The results for 3- and 4-layer Cut- and CG-FEM models can be found in figure 6.14.

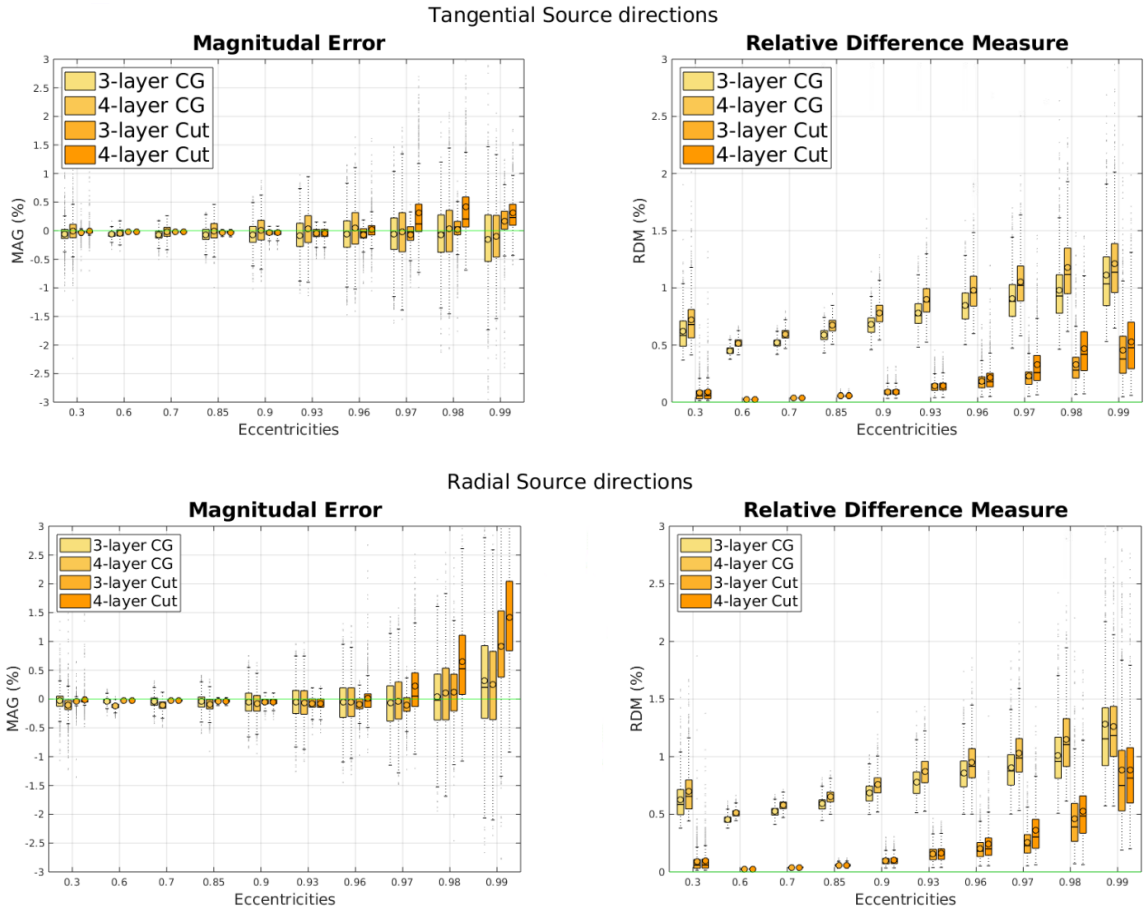

Fig. 6.14.: Overview of different EEG-errors for 3- and 4-layer CG- and CutFEM. Top: Errors for tangential source directions. Bottom: Errors for radial source directions. Errors are in percent and grouped by eccentricities. The green line marks optimal error values, the circle represents the average error.

Notice first that of all tested methods over all eccentricities only one upper quartile narrowly exceeded 2 percent and the highest overall error for a 4-layer model was 5.8 percent. All methods thus yielded very reliable results. For CutFEM it is noticeable that up to an eccentricity of 0.96, a distance to the skull of less than 1.2 mm, the 3- and 4- CutFEM models yielded virtually indistinguishable results across the different categories. Shifting the inner sphere thus had no effects at all on sources that were more than 1.2 mm away from the skull. It can also be noted that these very low errors indicate that the employed St. Venant source model can yield an excellent approximation of a dipolar source term. At higher eccentricities, for tangential RDM's the IQR increases from 0.06 to 0.41 for the 4-layer model and from 0.06 to 0.32 for its 3-layered counterpart. The largest differences were observed for radial MAG errors at an eccentricity of 0.97. Here the IQR difference was 0.35, a factor of 2.45. The highest overall error are similar at 4.8 and 4.9 respectively. The most notable difference is an increase in average MAG error in the 4-layer model, up to 1.6 percent for radial sources at eccentricity 0.99.

For CG-FEM, the MAG errors for 3- and 4-layer model are mostly identical, the RDM

errors feature similar IQR's but the average error is around 0.1 percent higher for the 4-layer model. This difference is mostly constant throughout all eccentricities and both source directions, indicating that for CG-FEM, in contrast to CutFEM, the shift has a slight impact on sources throughout the brain compartment.

There are three main differences in the results for CG- and CutFEM. The first is that CutFEM shows barely any errors at low eccentricites, with IQR's being lower by a factor of 3 to 18 than for CG-FEM. Over all eccentricities, CutFEM has similar or lower IQR's and maximal errors over all categories. The second difference is that CG-FEM has an average RDM-error that is 0.6 percent higher than CutFEM's. This difference changes little over eccentricities and source directions. Lastly, the MAG error for radial source directions at eccentricities over 0.98 shows similar IQR's and maximal errors for Cut- and CG-FEM but the average and median error are a little over 1 percent higher for CutFEM. This is the only category in which CutFEM is slightly outperformed by its tetrahedral counterpart and also the largest overall difference between the two methods.

tDCS

For tDCS, the setup is again very similar. The same points at the same eccentricities as in the EEG-subsection are examined in addition to a set of 899 skull points. The latter have a distance of less than 1 mm to the brain and less than 20 mm to the point of contact.

The results can be seen in figure 6.15. Again similarities to the EEG-case are immediately apparent. CutFEM shows barely any deviations at eccentricities below 0.97. The differences for CG are in the tenth of percents/degrees, though steadily increasing with eccentricity. That is, up to an ecc. of 0.98, where the proximity to the densely meshed CSF-compartment probably benefits the 4-layer compartment. Vector angle distribution is almost identical for Cut- and CG-FEM, with the latter being higher by about 0.05 to 0.1 degrees. Errors only increase notably at eccentricities larger than 0.99, the methods remaining almost identical with regard to angles. The average MAG error for CutFEM here is higher by about 0.53 percent while the IQR is half that of CG. Notably, these differences are significantly lower than the deviations in the directly adjacent skull compartment. In this group, 4-layer CutFEM shows its lowest overall errors with an angle IQR of 0.14 and a maximum of 0.85. CG-FEM on the other hand still has errors in the range and above of the 0.99 eccentricity group, with angle IQR and maximum being around 4.5 times higher. The 4-layer CG-FEM outperforming the 3-layer version in the skull domain. This however is probably due to the absence of the finely meshed CSF and a slight difference in resolution used for the respective skull compartments.

Overall, for randomly selected evaluation points, CutFEM slightly outperforms CG-FEM, but especially at lower eccentricities, the lead is not as strong as it is for EEG. A reason for this might be the the location of each each evaluation point within its containing fundamental mesh cell. To investigate this further, 1000 randomly chosen interior (non-scalp) cells are selected. Within each of those, 28 evaluation points are placed at regular intervals. Analytical and numerical current densities are computed and compared with regard to each points distance from the cell center. The results can be found in 6.16. Clearly, points that lie more eccentric within their cells feature higher errors, suggesting that one should restrict

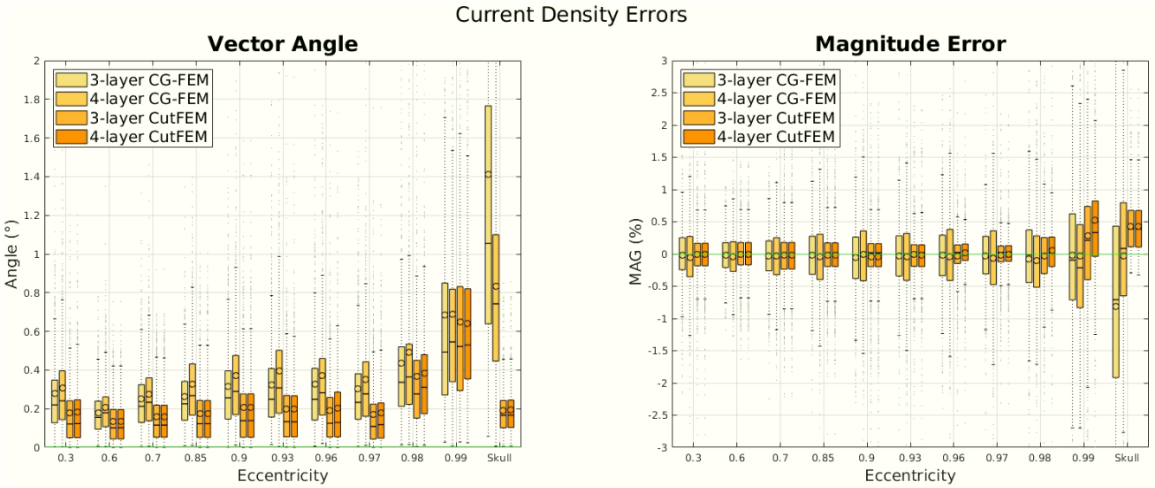

Fig. 6.15.: Overview of different tDCS-errors for 3- and 4-layer CG- and CutFEM. Right: Vector Magnitude differences in percent. The green lines indicate optimal values, the circle depicts the average error per category.

the feasible evaluation space to the cell centers. A reason why this effect was not observed for the EEG may lie in the usage of a distributed source model that is not restricted to one point alone, but rather the entire cell. Also, in tDCS the gradients of the potential are evaluated, not the potential itself. A similar gain in performance can be achieved for CG-FEM.

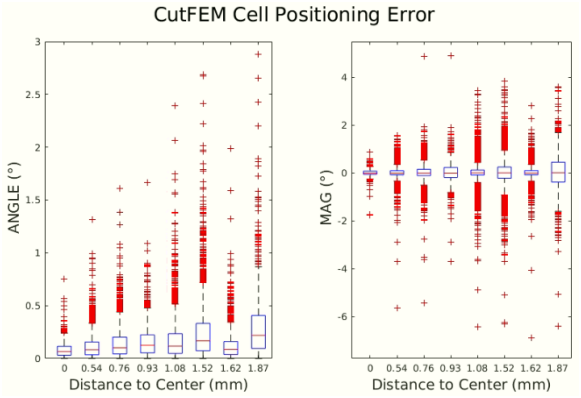

Fig. 6.16.: Dependence of CutFEM approximation on positioning inside fundamental mesh cell. Left: Angles for different distances from the cell center. Right: Magnitude errors. red crosses indicate outlier values.

Using the cell centers, we can get a more volumetric impression of the error distribution for 4-layer CG- and CutFEM. Figure 6.17. shows a cross-section of the area near the point of contact, portraying analytical and numerical current density vectors. Evaluation points are fundamental mesh centers. As can be seen, for both methods the vectors point in nearly the exact same direction throughout brain and skull compartment. The only noticeable differences are near the electrode on the scalp. Here, both methods vary distinctly from the analytical solution.

As the vectors in the graphic are not scaled by magnitude, the distribution of MAG er-

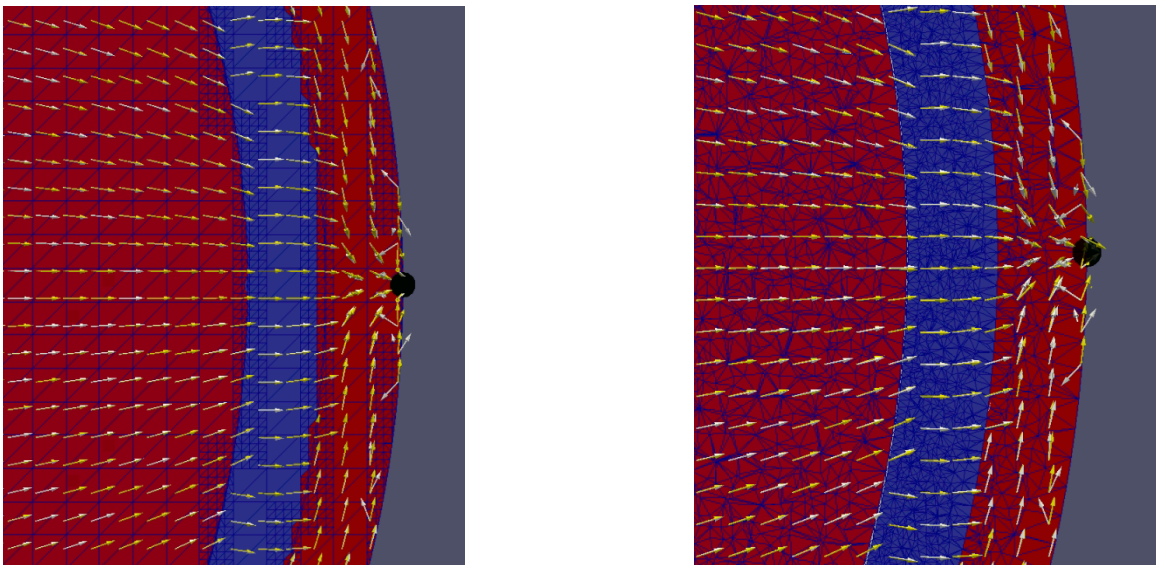

a) CutFEM b) CG-FEM

Fig. 6.17.: Depiction of analytical and numerical current density vectors. White arrows indicate the analytical solution, yellow the numerical. Arrows are superimposed. In places where only one arrow colour is visible, the two solutions point in the same direction. Vectors are not scaled by magnitude. The black dot indicates the sink electrode, the blue compartment is the skull layer. The black grid in the background represents the fundamental/tetrahedral mesh.

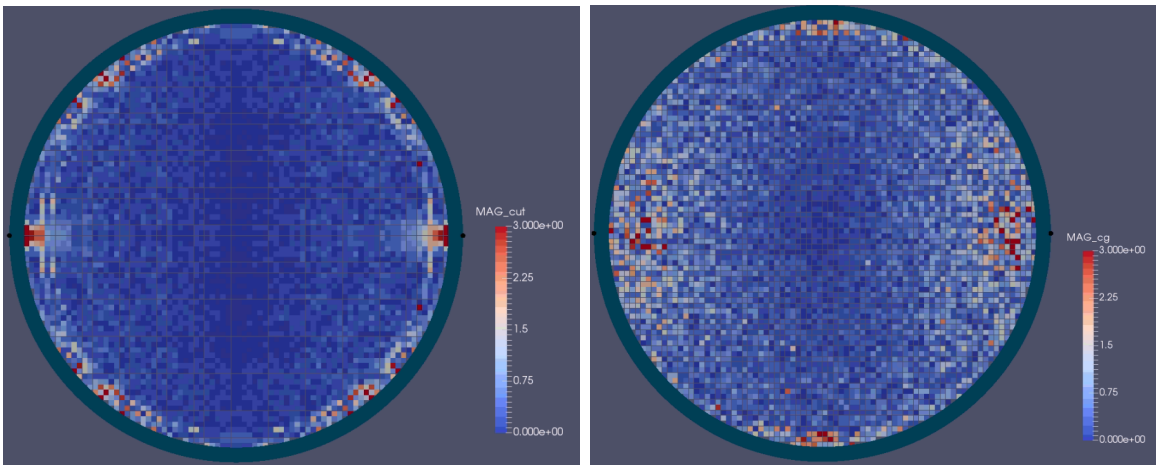

a) CutFEM b) CG-FEM

Fig. 6.18.: Comparison of absolute MAG errors for Cut- and CGFEM. Left: CutFEM. Right: CG-FEM. Fundamental mesh cells are colorised by MAG at the center. For a clearer comparison, the CG-errors stem from the nearest tetrahedral center, the MAG error at that point was then used to colorize the fundamental cell. Brightest color is reached at 3 percent. Scalp cells are ignored to improve clarity. Instead, the entire scalp area is depicted as single color sphere. Black dots indicate stimulation electrodes.

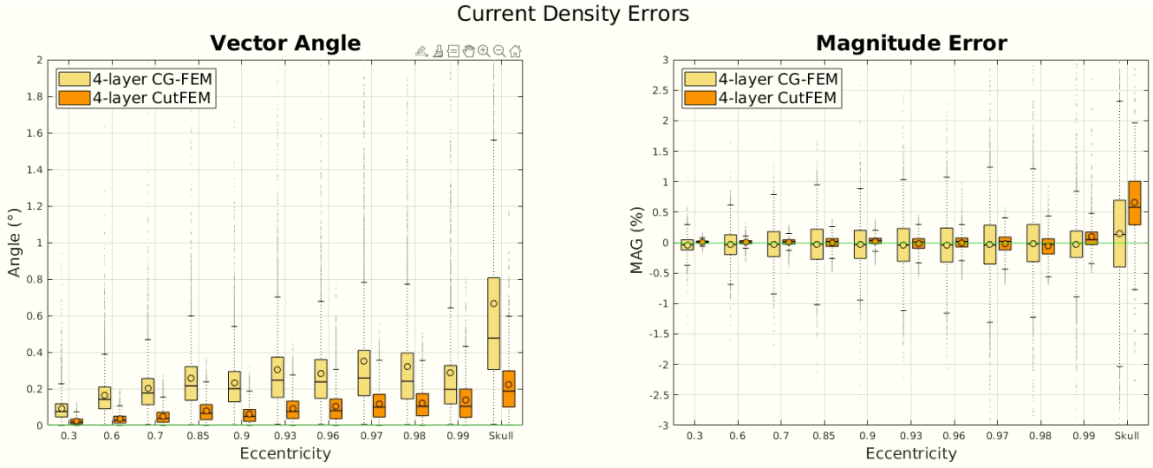

Fig. 6.19.: Overview of different tDCS-errors for 3- and 4-layer CG- and CutFEM taken at element centers. Right: Vector Magnitude differences in percent. The green lines indicate optimal values, the circle depicts the average error per category.

rors throughout the cross-section is visualized in figure 6.18. Current densities are again computed for the center point of each fundamental mesh cell and each cell was colorized with respect to the size of the MAG error at the center. For each fundamental mesh center point, the nearest tetrahedral center was located for the CG-method. Scalp cells were left out to improve clarity. Strikingly, CutFEM shows significantly better results this time. The highest absolute MAG error in the brain is 2.6 percent for CutFEM and 6.6 for CG-FEM. Additionally, high errors in the brain compartment are limited to cells that are cut by level-sets, whether there is a conductivity jump or not, indicating further potential for penalty parameter optimization. Overall, the high errors near the electrodes do not pervade through the skull into the brain. The same cannot be said for CG-FEM. Here, the electrodes have a much more pronounced influence on the proximate part of the brain region. Tissue boundaries are of secondary importance.

While both methods gained from using element centers, the difference in performance is now much more pronounced than in the box plot study before. This can be seen in figure 6.19. The different sample size of about 10 000 to 260 000 may also have a slight impact on the different results. While there was barely any impact on the skull compartment errors, CutFEM now outperforms CG-FEM throughout the entire brain, with the highest relative difference at low eccentricities, where maximal errors and IQR for CutFEM are on average a tenth/third respectively of the CG-values. While errors increase with eccentricity, the methods do not deteriorate in the same way as the did for EEG.

Regarding computation time, computing Current densities for one pair of stimulation electrodes took about ten times (on average 127 minutes to 25) as long for CutFEM. This is due to the longer time required to set up the system matrix with its additional terms. As this has to be done only once, the relative difference reduces for a higher number of stimulation electrodes.

When looking at memory consumption, CutFEM required approximately 3.6 GB of RAM compared t0 19.3 for CG-FEM. This difference depends largely on the size of the system

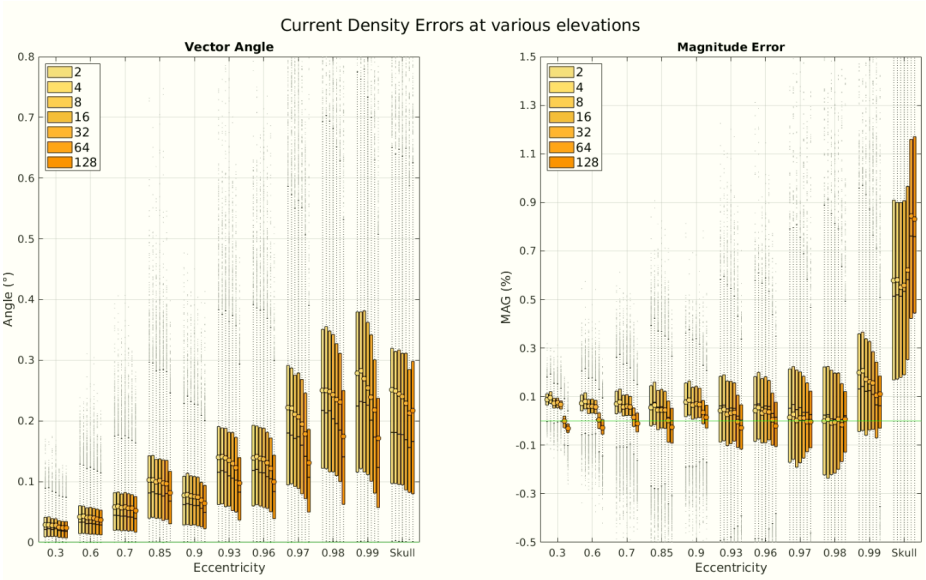

Fig. 6.20.: Comparison of CutFEM performance for different electrode positionings. Left: Vector angles in degrees. Right: Vector Magnitude differences in percent. The green lines indicate optimal values, the circle depicts the average error per category.

matrix and thus the number of degrees of freedom and was thus mostly constant throughout all examinations, whether for tDCS or EEG. Finally, the effects of electrode positioning on CutFEM forward results are examined. 8 source electrodes were placed at 2, 4, 8, 16, 32, 64, 128 degrees of elevation are placed on the scalp. Elevation is to be understood as angle between the vectors pointing from the scalp center to the point of contact and to the respective electrode. Corresponding sink electrodes are in the opposite way such that the point of contact is equidistant to the stimulation electrodes.

As the results in figure 6.20. show, a low distance between the stimulation electrodes leads to a slight overstating of the current density magnitude in the brain, especially at low eccentricities. Angles at low eccentricities are mostly unaffected, at eccentricities above 0.9, the results worsen by about 0.05 degrees on average. In contrast, the skull seems to be slightly better represented when the electrodes are closely together. All differences are very subtle, the highest difference lies in the skull area, where the proximate electrodes are about 0.25 percent better on average than the distant ones. Electrode positioning thus does not significantly impact on the performance of CutFEM.

To summarize the study, in both EEG and tDCS it was found that CutFEM outperforms CG-FEM in most categories examined. Both methods are highly accurate overall, with differences in low single-digit areas. The highest relative differences were found in the inner parts of the brain, with CutFEM having the highest advantage in EEG-RDM and both tDCS categories.

7. Summary and Outlook

The goal of this thesis was to test the Cut finite Element Method in a neuroscience scenario where skull and brain touch. As benchmark, a standard continuous Galerkin method with tetrahedrons was used. Introductions into the workings of both methods as well as the physiological background of both transcranial direct current stimulation and Electroencephalography were given in the early chapters. For CutFEM, two variants, using symmetrically and non-symmetrically weighted penalty terms were stated. This was followed by a short numerical analysis, were it was found that, when using the symmetric CutFEM variant, both FEM approaches can reach identical convergence rates. Additionally, the dependence of CutFEMs stability on two penalty parameters, Nitsche- and Ghost-penalty, was explained. These theoretical findings were examined in the following numerical studies.

Initially, a model was created that simulates the contact of brain and skull compartment while also featuring the availability of analytical solutions as benchmarks. The first two studies were then concerned with finding optimal contestants for a Cut- CG-FEM comparison. Mesh resolutions used were 2 mm for CutFEM and 1 mm for CG-FEM. First, the two CutFEM-variants with various penalty parameters were examined, which resulted in choosing the non-symmetric variant with corresponding penalty parameters. The reason for this was NWIPGs higher stability with regard to different penalty parameters alongside the fact, that its adjoint inconsistency, the reason for its slower theoretical convergence rate, can be neglected in the scenario at hand.

The second study compared two different tetrahedral meshing approaches, one used by the Zeffiro Interface and one delaunay-based from Gmsh. It was found that the more involved meshing algorithm of the latter was highly superior to Zeffiro. Furthermore, a possible correlation between the shape of a tetrahedron and numerical errors inside could not be proven.

After these preliminary studies, the third was concerned with the comparison of the two FEM-approaches. While both methods yielded very accurate results, CutFEM slightly outperfomed CG-FEM in most categories for both EEG and tDCS. The differences were most profound for the deeper parts of the brain. CutFEM also showed significantly less deviation from its 3-layer counterpart without touching skull and brain boundaries. With increasing eccentricity and decreasing distance to the point of contact, CutFEM was, for the most part, still slightly superior, but overall the methods' results became increasingly similar. For tDCS, it was found that the position and distance of the stimulation electrodes do not lead to significant changes in CutFEM's performance.

Computation times of CutFEM were similar in the EEG case but significantly higher for tDCS. CG-FEM had a memory consumption about 6 times higher than CutFEM, mostly due to its higher number of degrees of freedom.

Overall, CutFEM has shown promising results in this thesis, outperforming a standard

CG-FEM even at twice the resolution.

Outlook

In [Nüß18], it was found that the unfitted discontinuous Galerkin Method (UDG), a method that differs from CutFEM in the same way that CG-FEM differs from DG-FEM by allowing jumps not only over domain boundaries, but also mesh element boundaries, showed very similar results to CutFEM in a concentric sphere study. One might investigate whether UDG shows better performance than CutFEM in the categories where CutFEM differed the most from the 3-layer control model. Regarding other comparisons with different FEM-approaches, the tetrahedral CG-model that was used here is already among the most accurate fitted approaches that were tested in the literature, leaving little room for further investigation of the scenario presented in this thesis.

In the tDCS studies it was found that CutFEM has its largest errors in cells that are cut by level-sets, even if there was no conductivity jump. This suggests that there is room for further optimization of the penalty terms applied, either by modifying the parameters or by applying a different Ghost-penalty scheme.

Regarding the application in a realistic head model, this thesis has shown that slight geometric deformations like the one in the shifted sphere model have much less of an impact on distant regions of the model when using the CutFEM approach. This might indicate a better performance in models with many such deformations. Furthermore, segmentations from MRI-images rarely exceed 1 mm resolutions. It is at this point unclear whether this upper bound of resolution would have a stronger effect on the tetrahedral model from the CG-method or on the level-set approach from CutFEM.

To investigate this further, a possible modification of the model could use realistic CSF and brain tissue, still with identical conductivities, embedded in spherical skull and scalp compartments. This would maintain the existence of analytical solutions while providing the opportunity to investigate geometric deformations in brain areas that are not close to a large conductivity jump such as the one from skull to brain.

For modern tDCS-methods using multiple stimulation electrodes, CutFEM might show its largest advantage. Numerical errors were found to be largest near the stimulation electrodes. While errors throughout the model were lower for CutFEM, they most importantly did not pervade from the electrode position through the skull into brain. CG-FEM showed much higher errors here. While the CG-FEM errors are still very reasonable, these higher errors in the brain might accumulate and thus lead to significantly different inverse results. Such a deviation might be a topic of interest for further investigation.

Bibliography

[ABCM02] Douglas Arnold, Franco Brezzi, Bernardo Cockburn, and Donatella Marini. Unified analysis of discontinuous galerkin methods for elliptic problems. *SIAM J. Numer. Anal.*, 39, 01 2002.

[BBE+11] P Bastian, M Blatt, C Engwer, R Klöfkorn S Kuttanikkad, and T Neubauer M Ohlberger O Sander. Dune distributed and unified numerics environment. *URL: http://www. dune-project. org*, 2011.

[BH12] Erik Burman and Peter Hansbo. Fictitious domain finite element methods using cut elements: Ii. a stabilized nitsche method. *Applied Numerical Mathematics*, 62(4):328 – 341, 2012. Third Chilean Workshop on Numerical Analysis of Partial Differential Equations (WONAPDE 2010).

[BIA+04] Marom Bikson, Masashi Inoue, Hiroki Akiyama, Jackie Deans, John Fox, Hiroyoshi Miyakawa, and John Jefferys. Effect of uniform extracellular dc electric fields on excitability in rat hippocampal slices in vitro. *The Journal of physiology*, 557:175–90, 05 2004.

[BNB+12] Andre Russowsky Brunoni, Michael A. Nitsche, Nadia Bolognini, Marom Bikson, Tim Wagner, Lotfi Merabet, Dylan J. Edwards, Antoni Valero-Cabre, Alexander Rotenberg, Alvaro Pascual-Leone, Roberta Ferrucci, Alberto Priori, Paulo Sergio Boggio, and Felipe Fregni. Clinical research with transcranial direct current stimulation (tdcs): Challenges and future directions. *Brain Stimulation*, 5(3):175 – 195, 2012.

[BPV+15] M. Bauer, S. Pursiainen, J. Vorwerk, H. Köstler, and C. H. Wolters. Comparison study for whitney (raviart–thomas)-type source models in finite-element-method-based eeg forward modeling. *IEEE Transactions on Biomedical Engineering*, 62(11):2648–2656, 2015.

[Bra07] Dietrich Braess. *Finite elements: Theory, fast solvers, and applications in solid mechanics*. Cambridge University Press, 2007.

[Bur10] Erik Burman. Ghost penalty. *Comptes Rendus Mathematique*, 348(21-22):1217–1220, 2010.

[CS06] Bruno Cessac and Manuel Samuelides. Chapter 1: From neuron to neural networks dynamics. *The European Physical Journal Special Topics*, 142, 09 2006.

[CVWK15] Jae-Hyun Cho, Johannes Vorwerk, Carsten H. Wolters, and Thomas R. Knösche. Influence of the head model on eeg and meg source connectivity analyses. *NeuroImage*, 110:60 – 77, 2015.

[CZ98] Zhiming Chen and Jun Zou. Finite element methods and their convergence for elliptic and parabolic interface problems. *Numerische Mathematik*, 79:175–202,

01 1998.

[DM88] JC De Munck. The potential distribution in a layered anisotropic spheroidal volume conductor. *Journal of applied Physics*, 64(2):464–470, 1988.

[DMP+93] JC De Munck, Maria J Peters, et al. A fast method to compute the potential in the multisphere model. *IEEE Trans. Biomed. Eng*, 40(11):1166–1174, 1993.

[DMWC12] Jan De Munck, Carsten Wolters, and Maureen Clerc. *EEG and MEG: forward modeling*, pages 192–248. 01 2012.

[DPE12] Daniele Di Pietro and Alexandre Ern. *Mathematical Aspects of Discontinuous Galerkin Methods*, volume 69. 01 2012.

[EN17] Christian Engwer and Andreas Nüßing. Geometric reconstruction of implicitly defined surfaces and domains with topological guarantees. *ACM Transactions on Mathematical Software (TOMS)*, 44(2):1–20, 2017.

[Eva14] Lawrence C. Evans. *Partial differential equations*. Graduate studies in mathematics, v. 19. American Mathematical Society, 2nd ed. edition, 2014.

[EVLW17] Christian Engwer, Johannes Vorwerk, Jakob Ludewig, and Carsten H Wolters. A discontinuous galerkin method to solve the eeg forward problem using the subtraction approach. *SIAM Journal on Scientific Computing*, 39(1):B138–B164, 2017.

[FET00] T.C. Ferree, K.J. Eriksen, and D.M. Tucker. Regional head tissue conductivity estimation for improved eeg analysis. *IEEE Transactions on Biomedical Engineering*, 47(12):1584–1592, 2000.

[Fli05] Torsten Fließbach. Lehrbuch zur theoretischen physik ii. *Statistische Physik, Spektrum Akademie-Verlag*, 2005.

[Fou20] Zafeirios Fountas. Imperial college spiking neural networks for human-like avatar control in a simulated environment. 12 2020.

[FRM+10] Brita Fritsch, Janine Reis, Keri Martinowich, Heidi M Schambra, Yuanyuan Ji, Leonardo G Cohen, and Bai Lu. Direct current stimulation promotes bdnf-dependent synaptic plasticity: potential implications for motor learning. *Neuron*, 66(2):198–204, 2010.

[FW20] Torsten Fließbach and Hans Walliser. Elektrodynamik. In *Arbeitsbuch zur Theoretischen Physik*, pages 143–309. Springer, 2020.

[GHH07] Emmanuil Georgoulis, Edward Hal, and Paul Houston. Discontinuous galerkin methods for advection-diffusion-reaction problems on anisotropically refined meshes. *SIAM Journal on Scientific Computing*, 30, 01 2007.

[GMH+20] Benjamin C. Gibson, Teagan S. Mullins, Melissa D. Heinrich, Katie Witkiewitz, Alfred B. Yu, Jeffrey T. Hansberger, and Vincent P. Clark. Transcranial direct current stimulation facilitates category learning. *Brain Stimulation*, 13(2):393 – 400, 2020.

[GR09] Christophe Geuzaine and Jean-François Remacle. Gmsh: A 3-d finite element mesh generator with built-in pre-and post-processing facilities. *International journal for numerical methods in engineering*, 79(11):1309–1331, 2009.

[HH02] Anita Hansbo and Peter Hansbo. An unfitted finite element method, based on nitsche's method, for elliptic interface problems. *Computer methods in applied mechanics and engineering*, 191(47-48):5537–5552, 2002.

[HH09] Suzana Herculano-Houzel. The human brain in numbers: a linearly scaled-up primate brain. *Frontiers in Human Neuroscience*, 3:31, 2009.

[HHI+93] Matti Hämäläinen, Riitta Hari, Risto J. Ilmoniemi, Jukka Knuutila, and Olli V. Lounasmaa. Magnetoencephalography—theory, instrumentation, and applications to noninvasive studies of the working human brain. *Rev. Mod. Phys.*, 65:413–497, Apr 1993.

[HRP19] Qin He, Atena Rezaei, and Sampsa Pursiainen. Zeffiro user interface for electromagnetic brain imaging: A gpu accelerated fem tool for forward and inverse computations in matlab. *Neuroinformatics*, pages 1–14, 2019.

[HVG+07] Hans Hallez, Bart Vanrumste, Roberta Grech, Joseph Muscat, Wim Clercq, Anneleen Vergult, Yves D'Asseler, Kenneth Camilleri, Simon Fabri, Sabine Huffel, and Ignace Lemahieu. Review on solving the forward problem in eeg source analysis. *Journal of neuroengineering and rehabilitation*, 4:46, 02 2007.

[Jac07] John David Jackson. *Classical electrodynamics*. John Wiley & Sons, 2007.

[KK09] Timo Kirschstein and Rüdiger Köhling. What is the source of the eeg? *Clinical EEG and Neuroscience*, 40(3):146–149, 2009. PMID: 19715175.

[Kra19] Judith Kramps. Numerische Untersuchungen zu den Auswirkungen der quellmodelle auf das FEM-basierte MEG-Vorwärtsproblem. Master's thesis, WWU Münster, http://www.sci.utah.edu/ wolters/Paper-Wolters/2019/MasterKramps.pdf, 2019.

[LB86] Designationus SCRIBONIUS LARGUS and Joannes Michael BERNHOLD. *De compositionibus medicamentorum.* 1786.

[MLS+15] Takfarinas Medani, David Lautru, Denis Schwartz, Zhuoxiang Ren, and Gérard Sou. Fem method for the eeg forward problem and improvement based on modification of the saint venant's method. *Progress In Electromagnetics Research*, 153:11–22, 2015.

[NBFPL09] Michael A Nitsche, Paulo S Boggio, Felipe Fregni, and Alvaro Pascual-Leone. Treatment of depression with transcranial direct current stimulation (tdcs): a review. *Experimental neurology*, 219(1):14–19, 2009.

[Nit71] Joachim Nitsche. Über ein variationsprinzip zur lösung von dirichlet-problemen bei verwendung von teilräumen, die keinen randbedingungen unterworfen sind. In *Abhandlungen aus dem mathematischen Seminar der Universität Hamburg*, volume 36, pages 9–15. Springer, 1971.

[NPS+19] Andreas Nüßing, Maria Carla Piastra, Sophie Schrader, Tuuli Miinalainen, Sampsa Pursiainen, Heinrich Brinck, Carsten H. Wolters, and Christian Engwer. duneuro - A software toolbox for forward modeling in neuroscience. *CoRR*, abs/1901.02874, 2019.

[Nüß18] Andreas Nüßing. *Fitted and unfitted finite element methods for solving the EEG forward problem.* PhD thesis, Universität Münster, 2018.

[OFMS11] Robert Oostenveld, Pascal Fries, Eric Maris, and Jan-Mathijs Schoffelen. Fieldtrip: open source software for advanced analysis of meg, eeg, and invasive electrophysiological data. *Computational intelligence and neuroscience*, 2011, 2011.

[PBR+98] Alberto Priori, Alfredo Berardelli, Sabine Rona, Neri Accornero, and Mario Manfredi. Polarization of the human motor cortex through the scalp. *Neuroreport*, 9(10):2257–2260, 1998.

[PH67] R. Plonsey and D. B. Heppner. Considerations of quasi-stationarity in electrophysiological systems. *The Bulletin of mathematical biophysics*, 29 4:657–64, 1967.

[PVW16] Sampsa Pursiainen, Johannes Vorwerk, and Carsten H Wolters. Electroencephalography (eeg) forward modeling via h (div) finite element sources with focal interpolation. *Physics in Medicine & Biology*, 61(24):8502, 2016.

[Sch17] Benedikt Schott. *Stabilized cut finite element methods for complex interface coupled flow problems*. PhD thesis, Technische Universität München, 2017.

[She02] Jonathan Richard Shewchuk. What is a good linear finite element? interpolation, conditioning, anisotropy, and quality measures (preprint). 2002.

[SV+55] B de Saint-Venant et al. Mémoire sur la torsion des prismes. *Mémoires des Savants étrangers*, 14:233–560, 1855.

[Tch96] Evgueni Tcherniaev. Marching cubes 33: Construction of topologically correct isosurfaces. 01 1996.

[VCR+14] Johannes Vorwerk, Jae-Hyun Cho, Stefan Rampp, Hajo Hamer, Thomas R Knösche, and Carsten H Wolters. A guideline for head volume conductor modeling in eeg and meg. *NeuroImage*, 100:590–607, 2014.

[VHWG19] Johannes Vorwerk, Anne Hanrath, Carsten H. Wolters, and Lars Grasedyck. The multipole approach for eeg forward modeling using the finite element method. *NeuroImage*, 201:116039, 2019.

[Vog19] Nikolas Vogenauer. Sensitivity of tes optimization todifferent fem approaches. Master's thesis, WWU Münster, http://www.sci.utah.edu/ wolters/Paper-Wolters/2019/MasterVogenauer.pdf, 2019.

[WAT+06] C.H. Wolters, A. Anwander, X. Tricoche, D. Weinstein, M.A. Koch, and R.S. MacLeod. Influence of tissue conductivity anisotropy on eeg/meg field and return current computation in a realistic head model: A simulation and visualization study using high-resolution finite element modeling. *NeuroImage*, 30(3):813 – 826, 2006.

[WBW15] Sven Wagner, Martin Burger, and Carsten Wolters. An optimization approach for well-targeted transcranial direct current stimulation. *SIAM Journal on Applied Mathematics*, 76, 06 2015.

[WGH04] Carsten Wolters, Lars Grasedyck, and Wolfgang Hackbusch. Efficient computation of lead field bases and influence matrix for the fem-based eeg and meg inverse problem. *Inverse Problems*, 20:1099–1116, 08 2004.

[WKM+07] Carsten Wolters, Harald Köstler, Christian Möller, Jochen Härdtlein, Lars

Grasedyck, and Wolfgang Hackbusch. Numerical mathematics of the subtraction method for the modeling of a current dipole in eeg source reconstruction using finite element head models. *SIAM J. Scientific Computing*, 30:24–45, 01 2007.

[WRA+13] S Wagner, S M Rampersad, Ü Aydin, J Vorwerk, T F Oostendorp, T Neuling, C S Herrmann, D F Stegeman, and C H Wolters. Investigation of tDCS volume conduction effects in a highly realistic head model. *Journal of Neural Engineering*, 11(1):016002, dec 2013.

A. Appendix

A.1. Transfer-Matrix Approach

Calculating the Lead-Field is the most time consuming part of solving the EEG-Forward-Problem, especially if one requires many different source configurations (i.e. sets of sources in the brain). The goal of the Transfer Matrix Approach ([DMWC12], [WGH04]) is to set up a functional allowing the computation of different Lead-Fields by applying an easy to calculate source-term to it.

Let $b \in \mathbb{R}^{N_l}$ be a source term, $L \in \mathbb{R}^{N_e}$ the corresponding Lead-Field and $u \in \mathbb{R}^{N_l}$ the solution of the linear system $Au = b$. We are then looking for a matrix T s.t.

$$Tb = L = Eu, \tag{A.1}$$

where $E \in \mathbb{R}^{N_e x N_l}$ serves to evaluate the solution u at the position of the respective electrode (one column per electrode).

Since

$$u = A^{-1}b$$

we have

$$Tb = EA^{-1}b$$

and thus

$$T = EA^{-1} \Leftrightarrow AT^t = E^t, \tag{A.2}$$

where the symmetry of A was used.

The last equation can be solved column-wise, resulting in one column of the Transfer Matrix per electrode.

Note that this transfer matrix depends only on the positions of the electrodes on the scalp. It is set up independently of the sources placed inside the brain. Evaluating the Lead-Field of any source configuration reduces to computing the source vectors and a Matrix-Vector multiplication, allowing for thousands of sources to be used in solving the Inverse Problem. Now however, setting up the Transfer Matrix is the most time consuming step in the forward problem.

A.2. St. Venant Source Model

The (monopolar) St. Venant approach([MLS+15]) approximates a dipolar source term by placing monopoles in an area around the source location. More precisely, the goal is to find $N \in \mathbb{N}$ charges q_i at positions $x_i \in \mathbb{R}^3$ that maintain a variance of the multipole expansion of an electric potential resulting from a dipolar term $M\nabla\delta_{x_{dip}}$.

The n-th central moment of the expansion can be written as

$$S_n(f) = \int_\Omega (x - x_{dip})^n f(x) dx. \tag{A.3}$$

Note that starting from the third term this is not the Taylor expansion of an electric potential known from physics([Jac07]). Usage of the given formula is due to the historic formulation of the St. Venant Approach from 1855 which was used in elasticity theory([SV+55]).

For an approach that uses a more accurate series expansion, see ([VHWG19]).

Inserting the formula for the dipolar source into the expansion yields

$$S_n(M\nabla\delta_{x_{dip}}) = \int_\Omega (x - x_{dip})^n M\nabla\delta_{x_{dip}} dx$$

$$= -\int_\Omega n\nabla(x - x_{dip})^{n-1} M\delta_{x_{dip}} dx = -Mn(x - x_{dip})^{n-1}|_{x=x_{dip}}$$

Thus,

$$S_n(M\nabla\delta_{x_{dip}}) = \begin{cases} -M, \ n = 1 \\ 0, \ else. \end{cases} \tag{A.4}$$

On the other hand, our set of monopoles $\rho = \sum_{i=1}^N q_i\delta_{x_i}$ results in

$$S_n(\rho) = \int_\Omega (x - x_{dip})^n \sum_{i=1}^N q_i\delta_{x_i} dx = \sum_{i=1}^N \int_\Omega q_i(x - x_{dip})^n \delta_{x_i} dx$$

$$= \sum_{i=1}^N q_i(x - x_{dip})^n.$$

The locations for the monopoles depend on the discretization scheme, usually the surrounding vertices for a fitted FEM-approach. For CutFEM one might use the nodes of the fundamental mesh, however this might lead to the monopoles being in different compartments as the fundamental mesh contains no information about the head geometry.

Instead the nodes are placed inside the elements, allowing only elements that contain cut-cells of the source compartment. The exact locations are chosen based on a Gauss-Legendre quadrature of a freely choosable order.

Thus, after selecting monopole locations, it remains to calculate the charges q_i in a way such that

$$S_n(M\nabla\delta_{x_{dip}}) = S_n(\rho) \tag{A.5}$$

for all n up to a certain order. *Duneuro* also allows for n to be a multiindex by enabling mixed moments, achieving more accurate results. ([Nüß18])

Writing $(A.5)$ in matrix shape using $x_{ij} = S_n(\rho)$ yields

$$e_2 - X\rho = 0,$$

where e_2 contains a 1 as second entry and zeros everywhere else.

As there are usually more monopoles to be set than expansion terms, the problem is ill-posed. To alleviate this, Tikhonov-Regularization is employed, yielding a minimization problem of the Form

$$\underset{\rho}{\operatorname{argmin}} ||e_2 - X\rho||_2^2 + \lambda||W\rho||_2^2, \tag{A.6}$$

where $W_{i,i} = ||\frac{x_{dip}-x_i}{C}||^s$, with $s \in (0,1)$ and some constant C. This weighs the strength of a monopole with its distance to the dipole, resulting in a larger penalty for stronger monopoles further away from the dipole. A large s increases this effect, a smaller one dampens it. (A.6) can be written as

$$(X\rho - e_2)^T(X\rho - e_2) + \lambda(W^TW\rho + (W\rho)^TW).$$

Differentiation with regard to ρ yields

$$\begin{aligned} &X^Te_2 + e_2^TX - X^TX\rho - (X\rho)^TX + \lambda(W^TW\rho + (W\rho)^TW) \\ &= 2X^Te_2 - 2X^TX\rho + 2\lambda W^TW\rho \overset{!}{=} 0. \end{aligned}$$

Thus the problem reduces to solving the equation system

$$X^Te_2 = (\lambda W^TW + X^TX)\rho. \tag{A.7}$$

The St. Venant approach is the primary source model that is employed throughout this thesis. The parameters used throughout this thesis can be found below.

```
'type' : 'patch_based_venant';
'initialization' : 'closest_vertex',
'intorderadd' : '2',
'intorderadd_lb' : '2',
'numberOfMoments' : '3',
'referenceLength' : '20',
'relaxationFactor' : '1e-6',
'restrict' = 'true',
'weightingExponent' : '1',
'mixedMoments' : 'true',
'quadratureRuleOrder' : '2',
'compartment' : '3',
'scalePointsToBBox' : 'true'
'subtract_mean' : 'true',
'reduction' : '1e-15'
```

A.3. Analytical solutions

We now shortly discuss analytical solutions for tDCS and EEG.

tDCS

Assuming a compartment-wide constant conductivity tensor, we obtain

$$0 = \nabla\sigma\nabla u = \sigma\Delta u$$

for the electric potential u, ignoring boundary conditions for the moment. Introducing spherical coordinates yields

$$\Delta u = \frac{1}{r^2}\frac{\partial}{\partial r}(r^2\frac{\partial u}{\partial r}) + \frac{1}{r^2 sin\theta}\frac{\partial}{\partial\theta}sin\theta\frac{\partial u}{\partial\theta} + \frac{1}{r^2 sin^2\theta}\frac{\partial^2}{\partial\phi^2}.$$

As we are only interested in two scalp electrodes, the potential there is independent of ϕ. The last term is therefore equal to zero. Next, separation by variables yields $u(r,\theta) = R(r)\Theta(\theta)$, with

$$\frac{1}{R}\frac{\partial}{\partial r}(r^2\frac{\partial R}{\partial r} = -\frac{1}{\Theta sin\theta}\frac{\partial}{\partial\theta}sin\theta\frac{\partial\Theta}{\partial\theta}$$

Both sides are independent of the others' variable, allowing us to search for solutions independently by setting the right/left side respectively to a constant. This constant cannot be chosen freely, as the right side is periodical and regularity over the boundary require it to be $l(l+1)$ for some $l \in \mathbb{N}$. The equations then read

$$\frac{1}{R}\frac{\partial}{\partial r}(r^2\frac{\partial R}{\partial r} = l(l+1), \tag{A.8}$$

and

$$\frac{1}{\Theta\sin\theta}\frac{\partial}{\partial\theta}\sin\theta\frac{\partial\Theta}{\partial\theta} = -l(l+1). \tag{A.9}$$

The first equation can be solved by r^l and $\frac{1}{r^{l+1}}$, yielding a general solution

$$R_l(r) = A_l r^l + B_l\frac{1}{r^{l+1}}$$

The solution to the second equation is the l-th Legendre-polynomial P_l. Using these, the general solution can then be found as a linear combination of these equations, yielding

$$u(r,\phi) = \sum_{n=0}^{\infty} A_l r^l + B_l r^{-l+1})P_l\cos\theta. \tag{A.10}$$

Coordinate rotations and linear superposition can be used to derive the solution in a 4-layer sphere model for two electrodes at r_1, r_2 in compartment i. with radius r_i

$$u^i(r,\phi) = \sum_{n=0}^{\infty} A_l^i\frac{r_i}{r}^l + B_l^i\frac{r_i}{r}^{-l+1})(P_l(\theta_1) - P_l(\theta_2), \tag{A.11}$$

where θ_j is the angular distance of r and r_j. To derive the coefficients, boundary conditions on the tissue surfaces are imposed. These include continuity of both the potential and the outer normal of the current density. On the outermost boundary, the regular Neumann conditions are imposed. The boundary conditions thus yield an equation system whose size corresponds to the number of unknowns in A.11, allowing analytical expressions for each. They can be found in [FET00].

EEG

The following is a brief summary of the derivation of the analytical EEG solution for concentric spheres done in [DM88]. Recall the first line of the EEG forward problem

$$\nabla\sigma\nabla u = \delta(x_0 - x) \tag{A.12}$$

for a dipolar source at x_0. A dipole can be considered as the limit of two monopoles, one positively and the other negatively charged, whose distance goes to zero. Where they in the same place, they would cancel and not produce a potential field. Considering the negative monopole's position as the dipole location, the potential field then describes the field that arises by the displacement of the positive monopole. It can thus be described as the gradient of the monopole potential with respect to the dipole location or in other words

$$u(x) = M\nabla_0 u_{mon}(x),$$

where M is the dipole moment, pointing from negative to positive monopole. We consider layered, symmetric sphere. In spherical coordinates, this means that the conductivity thus only depends on the radial coordinate r and can be split into radial conductivity $\epsilon(r)$ and tangential cond. $\nu(r)$). The potential at an electrode e on the scalp then depends on the sphere origin, the source location's spherical coord. r_0 and the angular distance $w_{0,e}$ from source point to electrode. Similar to the tDCS-case, it can be expressed using Legendre-Polynomials P_n as

$$4\pi u_{mon} = \sum_{n=0}^{\infty}(2n+1)R_n(r_0, r)P_n(cosw_{0,e}), \tag{A.13}$$

with R_n being the solution of

$$\frac{\partial}{\partial r}(r^2\epsilon(r)\frac{\partial}{\partial r}R_n(r_0, r)) - n(n+1)\nu(r)R_n(r_0, r) = \delta(r_0 - r). \tag{A.14}$$

The solutions to this equation can be computed analytically, yielding a quasi-analytic solution to the spherical problem. While the series converges rather slowly, especially for superficial sources, the process can be sped up by means of asymptotic approximation formulas. For more information, see [DMP$^+$93].

B. Mathematical Background

B.0.1. Sobolev Spaces and Lax-Milgram

In contexts like (2.1), where the differential operators only appear inside an integral, it has proven useful to employ a generalized version of the classical term of a derivative. This generalization defines differentiability of an entire function rather than being a pointwise statement.

Definition B.1 (Weak Derivative) *Let $\Omega \in \mathbb{R}^n$ open non-empty, $f, g \in L^1_{loc}(\Omega)$, $\alpha = (\alpha_1, ..., \alpha_n)$ a multiindex. Then g is called weak derivative of f, if*

$$\int_\Omega g(x)\phi(x)dx = \int_\Omega f(x)D^\alpha\phi(x)dx \;\; \forall\, \phi \in C_c^\infty. \tag{B.1}$$

Basically, this states that g is the derivative of f if using partial integration to shift the derivatives from ϕ to f results in g (Boundary terms can be omitted as ϕ has compact support). It can be shown that this weak derivative is identical to the classical one, if it exists.([Eva14])

Grouping all functions for which a weak derivative exists together results in Sobolev spaces

Definition B.2 (Sobolev Space) *Let $\Omega \in \mathbb{R}^n$ open, non-empty, $1 \leq p \leq \infty$, $k \in \mathbb{N}$. Then*

$$W^{k,p}(\Omega) = \{u \in L^p(\Omega) : \forall \alpha \in \mathbb{N}^n \text{ with } |\alpha| \leq k \text{ the weak derivative } D^\alpha u \in L^p(\Omega) \text{ exists}\}.$$

Defining

$$||u||_{W^{k,p}(\Omega)} = \begin{cases} \sum\limits_{|\alpha|\leq k} ||D^\alpha u||_{L^p(\Omega)} \;, p < \infty \\ \max\limits_{|\alpha|\leq k} ||D^\alpha u||_{L^\infty(\Omega)} \quad , p = \infty \end{cases}$$

as the norm over a Sobolev Space turns it into a Banach Space. Each of the summands is itself a semi-norm, denoted by

$$|u|_{W^{k,p}(\Omega)} = \sum_{|\alpha|=k} ||D^\alpha u||_{L^p(\Omega)}$$

For the special case $p = 2$, $H^k(\Omega) := W^{k,2}(\Omega)$ is also a Hilbert Space.

The latter result is useful when using Sobolev Spaces in the context of the Lax-Milgram theorem that proves existence and uniqueness of solutions to weakly formulated PDE's.

Theorem B.1 (Lax-Milgram) *Let H be a Hilbert space, $a : H \times H \to \mathbb{R}$ a continuous bilinear form that is coercive, i.e. $a(v, v) > \alpha||v||_H^2$ for each $v \in H$ and some $\alpha > 0$. Then for every $l \in H'(\Omega)$ there is a uniqe solution $u \in H$ such that*

$$a(u, v) = l(v) \;\; \forall v \in H. \tag{B.2}$$

Proof: *see [Bra07].* □

In the context of PDE's, l from the above theorem is often an integral over the boundary of Ω. In order to justify that it is part of $H^1(\Omega)'$ the trace operator is helpful.

Theorem B.2 (Trace Theorem) *Let $\Omega \subseteq \mathbb{R}^n$ have a Lipischitz boundary $\partial\Omega$. Then there exists a continuous linear map*

$$T : H^1(\Omega) \to H^{\frac{1}{2}}(\Omega) := \{u \in L^2(\partial\Omega) : \exists u \in H^1(\Omega) : Tu = v\}$$

with

$$Tu = u|_{\partial\Omega}$$

and

$$||Tu||_{H^{\frac{1}{2}}(\partial\Omega)} \leq C||u||_{H^1(\Omega)}$$

Proof: ([Bra07]) □

C. Implementation

Setting up and solving the linear equation systems is a resource-intense process. The distributed and unified numerics environment([BBE+11]) is a C++ -based open source software toolbox providing a fast and efficient solver environment for partial differential equations using the Finite Element Method. Based on DUNE, the institutes for bioelectromagnetism and applied mathematics in Münster collaborate on the development of duneuro, a toolbox to solve the forward problems for MEG, EEG and tDCS. Duneuro offers Matlab and python-bindings, allowing convenient access and evaluation via scripts even for users without experience with C++. Various FEM-approaches are currently implemented, the ones mentioned already in this thesis in addition to discontinuous Galerkin methods both for fitted and unfitted meshes. Duneuro

A part of the wwork leading up to this thesis lay in adapting duneuros CutFEM-approach to also be able to solve the tDCS forward problem. The following is a short overview of how to solve the tDCS forward problem in a single layer sphere model using CutFEM. For a detailed description on solving the EEG forward problem, see [NPS+19]. First, a driver needs to be created. It constitutes the base from which all following steps are executed. For CutFEM, the driver requires information about the fundamental mesh, level-sets and the used penalty scheme including penalty parameter choice. Additionally, one has to provide some information for the DUNE-solver.

```
config = {
'type' : 'unfitted',
'solver_type' : 'cut',
'compartments': 1,
'volume_conductor' : {
'grid' : {
'cells' : (30, 30, 30),
'upper_right' : (220, 220, 220),
'lower_left' : (30, 30, 30),
'refinements' : 2
}
},
'domain' : {
'domains' : ['brain'],
'level_sets' : ['outer_brain'],
'brain.positions' :  ['i'],
'csf_brain.radius' : 78,

},
'solver' : {
```

```
'conductivities' : [0.00033],
'edge_norm_type' : 'face',
'penalty' : 16,
'ghost-penalty' : 5e-3,
'intorderadd' : 0,
'reduction' : 1e-10,
'scheme' : 'sipg',
'weights' : 'tensorOnly',
'smoother' : 'default'
}
}
for k in config['domain']['level_sets']:
config['domain'][k] = {
'type' : 'sphere',
'center' : (127, 127, 127)
}
driver = dp.tDCSPointDriver3d(config)
```

This creates a fundamental mesh with 30 by 30 by 30 cubes, a spherical level set for the brain with center, radius and conductivity as stated, as well as a corresponding subtriangulation by applying the TPMC-algorithm twice. Once the driver has been created one proceeds by setting the electrode positions, embedding each one in a cut-cell.

```
electrodes = np.genfromtxt(filename_electrodes,delimiter=None)
electrodes = [dp.FieldVector3D(t) for t in electrodes.tolist()]
driver.setElectrodes(electrodes, {})
```

Computing the tDCS-Matrix now consists of two steps. First an Evaluation Matrix containing the coefficients of the finite element approximation is calculated via

```
solver_config = {
'solver.reduction' : 1e-12,
'solver.compartments' : 4
}
EvalMatrix = driver.computeEvaluationMatrix(solver_config)
```

The driver now sets up the system matrix and solves it using DUNE's ISTL-solver, applying algebraic multigrid preconditioning on the way. Finally, at the point of writing, one has the choice of returning the electric potential or its gradient at the fundamental mesh center points. Future versions will include current density vectors and arbitrary locations.

```
solution = driver.applyEvaluationMatrix(EvalMatrix,
 {'evaluation_return_type' : 'potential'})
```

Plagiatserklärung der / des Studierenden

Hiermit versichere ich, dass die vorliegende Arbeit über „CutFEM forward modeling for geometries with touching surfaces in bioelectromagnetism“ selbstständig verfasst worden ist, dass keine anderen Quellen und Hilfsmittel als die angegebenen benutzt worden sind und dass die Stellen der Arbeit, die anderen Werken – auch elektronischen Medien – dem Wortlaut oder Sinn nach entnommen wurden, auf jeden Fall unter Angabe der Quelle als Entlehnung kenntlich gemacht worden sind.

Münster, den 02.März 2021
Tim-René Erdbrügger

Ich erkläre mich mit einem Abgleich der Arbeit mit anderen Texten zwecks Auffindung von Übereinstimmungen sowie mit einer zu diesem Zweck vorzunehmenden Speicherung der Arbeit in eine Datenbank einverstanden.

Münster, den 02.März 2021
Tim-René Erdbrügger